UNIVERSIDADE FEDERAL DE SANTA CANTARINA
CENTRO TECNOLÓGICO DE JOINVILLE
CURSO ENGENHARIA AEROESPACIAL

THOMAS PEREIRA DO CARMO

ANALYSIS OF CHANNEL FLOW WITH A SQUARE OBSTACLE USING LBM: INVESTIGATION OF SECONDARY FREQUENCIES IN THE WAKE AT CRITICAL REYNOLDS REGIMES

Joinville
2025

THOMAS PEREIRA DO CARMO

ANALYSIS OF CHANNEL FLOW WITH A SQUARE OBSTACLE USING LBM: INVESTIGATION OF SECONDARY FREQUENCIES IN THE WAKE AT CRITICAL REYNOLDS REGIMES

Trabalho apresentado como requisito para obtenção do título de Bacharel em Engenharia Aeroespacial, no Curso de Engenharia Aeroespacial, do Centro Tecnológico de Joinville, da Universidade Federal de Santa Catarina.

Orientador: Dr. Diogo Nardelli Siebert

Coorientador: Dr. Ricardo Martins Leite Bazarin

Joinville

2025

THOMAS PEREIRA DO CARMO

ANALYSIS OF CHANNEL FLOW WITH A SQUARE OBSTACLE USING LBM: INVESTIGATION OF SECONDARY FREQUENCIES IN THE WAKE AT CRITICAL REYNOLDS REGIMES

Este Trabalho de Conclusão de Curso foi julgado adequado para obtenção do título de Bacharel em Engenharia Aeroespacial, no Curso de Engenharia Aeroespacial, do Centro Tecnológico de Joinville, da Universidade Federal de Santa Catarina.

Joinville (SC), 23 de fevereiro de 2025.

Banca Examinadora:

Documento assinado digitalmente
Diogo Nardelli Siebert
Data: 05/12/2025 16:53:22-0300
CPF: ***.839.959-**
Verifique as assinaturas em https://v.ufsc.br

Prof. Dr. Diogo Nardelli Siebert
Orientador/Presidente

Documento assinado digitalmente
JUAN PABLO DE LIMA COSTA SALAZAR
Data: 05/12/2025 17:38:46-0300
CPF: ***.810.379-**
Verifique as assinaturas em https://v.ufsc.br

Prof. Dr. Juan Pablo de Lima Costa Salazar
Membro(a)
UFSC

Documento assinado digitalmente
Luis Orlando Emerich dos Santos
Data: 05/12/2025 17:27:24-0300
CPF: ***.977.838-**
Verifique as assinaturas em https://v.ufsc.br

Prof. Dr. Luis Orlando Emerich dos Santos
Membro(a)
UFSC

This work is dedicated to my dear parents, Alexssandro and Claudia, whose support made this achievement possible.

ACKNOWLEDGEMENTS

First and foremost, I would like to thank my parents, Alexssandro and Claudia, who have always believed in my dreams and never let me give up on them. To my father, who has always been my source of inspiration through his persistence and discipline. To my mother, for always showing me that even in the midst of chaos and anxiety, calmness and patience can still exist, and that logic can be your best ally in such moments. To Sofia, who will always be my little sister and who gave me my first understanding of what it means to truly care for someone.

To my girlfriend, Beatriz Otsuzi, my special thanks. Thank you for being by my side all these years, supporting me in every decision. You have taught me, and continue to teach me, what it truly means to love.

To my dear grandfather, Lauro Pereira, for his example of perseverance and for teaching me that happiness lies in simple things, whose stories brightened my childhood.

To my families, Pereira and Carmo, for giving me a sense of belonging and warmth, no matter where I was in Brazil or in the world.

To the Otsuzi family, who came into my life through my beloved girlfriend and welcomed me with open arms from the very beginning, becoming my second family.

To my friend Luiz Prince, whom I met early in college and who, by chance, became my housemate and eventually a brother to me. Alongside him, my friends Pedro Hermes, Vanessa Tavares, Vinícius Soares, João Piretti, and Pedro Kiyoshi made university a lighter and happier place.

To my friends at LabCC, in special, Ricardo Bazarin, Christoph Zevenbergen and Bernardo Gehlen, who turned my scientific initiation into a joyful experience and helped me along the process of developing this work.

To my friends Pedro de Carvalho and Matheus Vitti, for being my brothers in Germany and companions in so many adventures.

To my friends from the TvK student residence — Akshdeep, Ben, Johannes, Scarlet, Samar, Naumann, Charlotte, Li-min, and Karl — thank you for making TvK a place I can truly call home.

To my friends at Fraunhofer ILT — Marcel, Felix, Finley, David, and Alex — for showing me that people who had never met before, from completely different cultures, can still build such deep bonds of friendship.

To my professor, Diogo Nardelli Siebert, for his trust, support, and guidance throughout the development of this work.

To all of you, my heartfelt thanks!

The most exciting phrase to hear in science, the one that heralds new discoveries, is not “Eureka” but “That’s funny..."

Isaac Asimov

RESUMO

O Método de Lattice Boltzmann (LBM) tem se destacado como uma ferramenta computacional eficiente para simulações em mecânica dos fluidos, especialmente em meios porosos e escoamentos imiscíveis. Entretanto, sua aplicação em escoamentos aerodinâmicos não alcançou o mesmo nível de sucesso observado nas áreas mencionadas. Isso ocorre devido a vários fatores, incluindo instabilidades numéricas em altos números de Reynolds, a ausência de modelagem de turbulência na formulação clássica do LBM e o uso intrínseco de malhas regulares e uniformes, que dificulta a representação de superfícies curvas. Além disso, estudos recentes comparando o LBM com o método de volumes finitos apontaram discrepâncias na formação de vórtices ao redor de cilindros quadrados, mesmo em condições laminares, nas quais métodos tradicionais revelam mais de uma frequência característica. Esse problema é particularmente relevante, pois não se enquadra teoricamente nos desafios comumente reconhecidos do método. Nesse contexto, o presente trabalho investiga os fatores que influenciam a precisão do LBM na simulação de escoamentos ao redor de cilindros quadrados em baixos números de Reynolds, com foco na formação e desprendimento de vórtices. Para isso, foi desenvolvida uma implementação computacional do LBM utilizando o conjunto de velocidades D2Q9. Diferentes tratamentos de condições de contorno foram avaliados para as regiões de entrada e saída do domínio, incluindo o esquema clássico proposto por Zou and He (1997), bem como abordagens alternativas, como condições convectivas, de extrapolação e de gradiente nulo. Diferentes formulações do operador de colisão também foram consideradas. Os resultados foram validados por meio de comparações com dados experimentais e simulações utilizando métodos como o Método de Volumes Finitos (FVM) e o Discrete Unified Gas Kinetic Scheme (DUGKS). A análise espectral do coeficiente de sustentação e o cálculo do número de Strouhal permitiram identificar as frequências associadas aos modos primário e secundário de vórtices. Esses achados fornecem insights importantes sobre as limitações do LBM na captura da formação e desprendimento de vórtices, especialmente em regimes transitórios, e destacam a influência das condições de contorno adotadas nesse tipo de problema.

Keywords: Lattice Boltzmann; obstaculo quadrado; condições de contorno;

ABSTRACT

The Lattice Boltzmann Method (LBM) has emerged as an efficient computational tool for simulations in fluid mechanics, especially in porous media and immiscible flows. However, its application to aerodynamic flows has not achieved the same level of success observed in the aforementioned areas. This is due to several factors, including: numerical instabilities at high Reynolds numbers, the lack of turbulence modeling in the classical LBM formulation, and the intrinsic use of regular and uniform grids, which hinders the representation of curved surfaces. Additionally, recent studies comparing LBM with the finite volume method have pointed out discrepancies in vortex formation around square cylinders, even under laminar conditions, where traditional methods reveal more than one characteristic frequency. This issue is particularly relevant, as it does not theoretically fall within the commonly recognized challenges associated with the method. In this context, the present work investigates the factors that influence the accuracy of LBM in simulating flows around square cylinders at low Reynolds numbers, focusing on vortex formation and shedding. For this purpose, a computational implementation of the LBM using the D2Q9 velocity set was developed. Different boundary condition treatments were evaluated for the inlet and outlet regions of the domain, including the classical scheme proposed by Zou and He (1997), as well as alternative approaches such as convective, extrapolation, and zero-gradient conditions. Different formulations of the collision operator were also considered. The results were validated through comparisons with experimental data and simulations using methods such as the Finite Volume Method (FVM) and the Discrete Unified Gas Kinetic Scheme (DUGKS). Spectral analysis of the lift coefficient and the calculation of the Strouhal number made it possible to identify the frequencies associated with the primary and secondary vortex modes. These findings provide important insights into the limitations of LBM in capturing vortex formation and shedding, especially in transitional regimes, and highlight the influence of the adopted boundary conditions on this type of problem.

Keywords: Lattice Boltzmann; square obstacle; boundary conditions;

LIST OF FIGURES

LIST OF CHARTS

LIST OF TABLES

CONTENTS

1 INTRODUCTION

The Lattice Boltzmann method (LBM) has established itself as an important computational tool for fluid mechanics simulation over complex geometries, with applications in aerodynamics, aeroacustics and turbulent flow (Mohamad, 2013; Succi, 2013; Guo; Shu, 2013; Krüger *et al.*, 2017). Developed from the kinetic theory of gases, the LBM has significant advantages in terms of computational efficiency and ease of implementation when compared to traditional methods based on the Navier-Stokes equations (Chen; Doolen, 1998; Schulz *et al.*, 2003; Geller *et al.*, 2006). Specifically in aerospace engineering, the LBM plays a central role by supporting the early-stage development of new components and aerodynamic surfaces, reducing prototyping costs, and accelerating design cycles. Within this context, the method has been adopted in aerospace applications, with tools such as PowerFLOW and OpenLB already employed to simulate aerodynamic flows. These developments demonstrate the method's practical effectiveness and maturity for aerospace-related analyses (Noelting; Fares, 2015; Romani; Casalino, 2017).

Despite its practical adoption, several challenges remain in aerodynamic applications, including numerical instabilities at high Reynolds numbers, the absence of turbulence modelling in its classical formulation, and the reliance on regular and uniform meshes, which limits the representation of curved surfaces (Hou *et al.*, 1996; Teixeira, 1998). These limitations become more pronounced in scenarios that require accurate boundary-layer resolution, robustness under high Mach regimes, or local mesh refinement, where alternatives such as adaptive lattice strategies or hybrid formulations are often necessary (Rohde *et al.*, 2006; Tran *et al.*, 2022). When applied to transient problems, as in the classic case of flow in a channel with an obstacle, the method also shows limitations in accurately capturing complex fluid dynamic phenomena, particularly regarding the formation and development of secondary vortical structures when reaching critical Reynolds numbers (Wang *et al.*, 2015).

Experiments with square section cylinders had already identified the formation of a second vortex oscillation mode, detaching from the trailing edge of the section (Bearman; Trueman, 1972; Okajima, 1982; Reyes *et al.*, 2013), and numerical analyses using conventional methods, such as Finite Volume Method (FVM), corroborate these results, identifying both the primary and secondary frequencies associated with these flow modes (Turki *et al.*, 2003).

Wang *et al.* (2015) demonstrated that the DUGKS method faithfully reproduced the previous numerical results. However, when applying the LBM to the same problem, Wang *et al.* (2015) observed a significant discrepancy, as the method failed to adequately capture the secondary structures and characteristic frequencies associated

with the critical Reynolds regimes from the comparison of the coefficients of lift (C_l) and drag (C_d) over time.

Previous studies have investigated the performance of the LBM in flows with vortex shedding. For example, Breuer *et al*. (2000) compared the LBM and the FVM for confined flow around a square cylinder (blockage ratio of 1/8), analyzing velocity profiles, drag coefficient, recirculation length, and Strouhal number over Reynolds numbers ranging from 0.5 to 300. This gap motivates further investigation, as other studies addressing different aspects of flow around square cylinders have also not focused on the direct impact of boundary conditions.

Other works that simulate flow around square cylinders using the Lattice Boltzmann Method (LBM) address different aspects of the problem, such as the comparison between different collision models, including Bhatnagar-Gross-Krook (BGK), Multi-Relaxation-Time (MRT), and DUGKS (Wang *et al*., 2015), the influence of the blockage ratio (Turki *et al*., 2003), or the detailed dynamics of vortex motion in confined flows (Suzuki *et al*., 1993). None of these works, however, isolate and examine the direct impact of the choice and implementation of boundary conditions on the vortex shedding process.

Thus, this work differs in that it specifically addresses the impact of the boundary conditions on the LBM's ability to represent secondary vortical structures, in comparison with experimental results and other numerical methods, such as FVM and DUGKS.

In this context, this work presents an evaluation of how boundary conditions influence the representation of oscillatory phenomena and includes the implementation of a dedicated LBM-based numerical solver designed for this problem. The study analyzes the impact of conditions such as Convective, First Order Extrapolation (FOE), Second Order Extrapolation (SOE), and Null Longitudinal Velocity Gradient on the simulation of flows in a channel with an obstacle, with the results validated against experimental data and simulations obtained using FVM and DUGKS.

1.1 OBJECTIVES

Establishing confidence in the correct modeling of laminar flows around square obstacles, both in terms of numerical formulation and boundary condition treatment, is an essential step before extending the analysis to turbulent-flow problems. In order to address the inconsistency of the LBM in reproducing secondary vortex modes in these laminar configurations, the following objectives are proposed.

1.1.1 General objective

To develop and validate a numerical simulation using the LBM, for the accurate reproduction of the secondary modes of vortices in critical flows around square obstacles, contributing to the improvement of the consistency of the method in this class of problems.

1.1.2 Specific Objectives

- Quantitatively characterize the formation and evolution of vortical structures in the transient regime of flow in a channel with a square obstacle;
- Compare the influence of using different collision operators, including BGK, MRT and Two-Relaxation-Time (TRT);
- Determine the frequency spectra associated with the primary and secondary modes of vortices using Fourier analysis;
- Implement and comparatively evaluate the performance of different outlet boundary condition schemes (Convective, First-Order Extrapolation, Second-Order Extrapolation, and Null Longitudinal Velocity Gradient) in reproducing the physical phenomenon;
- Propose recommendations for the selection of boundary conditions that favor the correct representation of vortical dynamics and characteristic secondary modes.

2 THEORETICAL BACKGROUND

In order to properly understand obstacle flow simulations using the LBM, it is essential to understand the physical and mathematical principles behind it. This chapter explores the essential concepts of fluid mechanics and the kinetic theory of gases, which are necessary for deriving the Lattice-Boltzmann equation and understanding its dynamics. In addition, the analysis and theoretical concepts for collision operators, streaming and boundary conditions makes it possible to evaluate the advantages and limitations of the method as for interpreting the simulation results.

2.1 FLUID MECHANICS

To mathematically model the motion of fluids, this section introduces the continuity and Navier–Stokes equations, which are derived from the principles of mass and momentum conservation. These equations rely on a continuum description of fluids and form the foundation of classical fluid mechanics.

2.1.1 Microscopic, Mesoscopic and Macroscopic Scales

Fluid dynamics can be analyzed at different scales, ranging from the individualized description of particle interactions to formulations that model the fluid as a continuum, depending on the underlying theory and the desired level of detail (Krüger *et al.*, 2017). These distinct modelling frameworks reflect how temporal and spatial scales influence the choice between microscopic, mesoscopic, and macroscopic descriptions of the flow.

On the microscopic scale, the behavior of the fluid is described by the individual movement of the molecules, based on particle mechanics. In contrast, on the macroscopic scale, the fluid is treated as a continuous medium where the average effects of collisions are considered through the transport coeffcients, like viscosity and condutivity, and its behavior is modeled by equations such as Navier-Stokes.

At the mesoscopic level, fluid behaviour is described within the framework of kinetic theory, in which the state of the system is represented by a particle distribution function governed by the Boltzmann equation. This formulation connects microscopic particle dynamics with macroscopic continuum variables through multiscale procedures such as the Chapman–Enskog expansion, which enables the recovery of the Navier–Stokes equations from the underlying kinetic description. Within this mesoscopic framework, the LBM emerges as a numerical approach that solves a discretized version of the Boltzmann equation on a lattice, where the evolution of the distribution function provides access to the macroscopic flow fields used in this work.

Given that each modeling regime resolves physical mechanisms within specific ranges of scale, the definition of temporal and spatial scales becomes an important element of the analysis. Ensuring consistency between these scales and the physical phenomena under investigation directly influences the accuracy of the predicted dynamics and the suitability of the numerical method for describing the flow.

In this context, the Knudsen number, presented in Equation 1, is a dimensionless parameter that indicates whether a flow can be accurately described by continuum mechanics or requires a kinetic formulation. It is defined as the ratio between the molecular mean free path (l_{mfp}) and a characteristic length scale of the flow (l), and therefore determines the validity of the continuum hypothesis and the regimes in which kinetic effects become significant.

$$Kn = \frac{l_{mfp}}{l} \tag{1}$$

The behavior of the fluid varies significantly depending on the value of the Knudsen number. For values of $Kn < 0.01$, the fluid operates in the continuous regime. When $0.01 \leq Kn < 0.1$, the flow enters the slip regime, developing sliding effects at solid interfaces that require modified boundary conditions for proper modeling (Krüger *et al.*, 2017).

At higher values ($0.1 \leq Kn < 10$), the fluid is in the transitional regime, where characteristics of both the continuum and molecular regimes coexist, making mesoscopic methods such as LBM particularly suitable. Finally, for $Kn \geq 10$, the flow reaches the free molecular regime, in which the particles move essentially without collisions, requiring microscopic approaches based on kinetic theory for their correct description. This multiscale perspective is fundamental to understanding how methods based on kinetic theory, such as LBM, can simulate classical fluid mechanics phenomena from statistical principles (Krüger *et al.*, 2017). Figure 1 and Table 1 summarizes the regimes discussed.

Figure 1 – Knudsen number and gas flow regimes

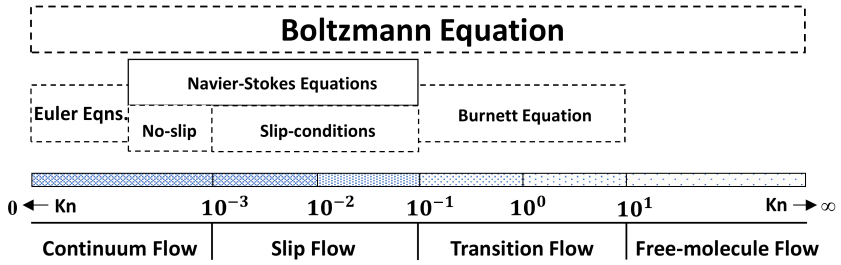

Source: Adapted from Zhao and Ji (2022, p.2).

In this way, understanding the different scales involved in fluid dynamics makes it possible to establish a conceptual bridge between microscopic and macroscopic ap-

Chart 1 – Classification of flow regimes according to Knudsen number

Value of Kn	**Type of model**
$Kn \to 0$	Inviscid flow (Euler equations).
$Kn \leq 0,001$	Continuous flow (Navier-Stokes-Fourier equations).
$0,001 \leq Kn \leq 0,1$	Slipping regime (Navier-Stokes equations with velocity slip and temperature jump as boundary conditions).
$0,1 \leq Kn \leq 10$	Transition regime (Boltzmann equations or particle methods such as DSMC).
$Kn \geq 10$	Free molecular path regime (particle methods such as DSMC).

Source: Author (2025).

proaches. Mesoscopic methods, such as LBM, make it possible to derive the equations governing the fluid's continuous behavior from the statistical foundations of kinetic theory. Using the Chapman-Enskog expansion, for example, it is possible to obtain expressions representing fundamental conservation laws from the simplified Boltzmann equation. Among these laws is the conservation of mass, expressed by the continuity equation, which is presented in the following subsection.

2.1.2 Continuity Equation

Assuming that the fluid behaves as a continuous medium, the analysis begins with the principle of mass conservation, which states that mass can neither be created nor destroyed (White, 2016). Consequently, any variation of mass in a fixed control volume must result exclusively from the entry or exit of mass through the boundaries of that volume.

This principle is represented in integral form by Equation 2:

$$\frac{\partial}{\partial t}\int_V \rho \mathrm{d}V = -\oint_{\partial V} \rho \boldsymbol{u} \cdot \mathrm{d}\boldsymbol{A} = -\int_V \nabla \cdot (\rho \boldsymbol{u})\, \mathrm{d}V \tag{2}$$

where ρ represents the density of the fluid, $\boldsymbol{u}$ is the velocity vector, and $\mathrm{d}\boldsymbol{A}$ is the area vector oriented outward from the control volume.

By applying the divergence theorem and considering an arbitrary control volume, the differential form of Equation 2 is obtained:

$$\frac{\partial \rho}{\partial t} + \nabla \cdot (\rho \boldsymbol{u}) = 0 \tag{3}$$

which locally expresses the conservation of mass in a flowing fluid.

2.1.3 Navier-Stokes equation

Based on Newton's second law, the Navier–Stokes equation expresses the rate of change of momentum inside a control volume as the balance between the mo-

mentum flux through its boundaries and the external forces acting on the fluid. This formulation distinguishes contact forces, represented by pressure and viscous stresses on the control surface, from body forces distributed volumetrically, both of which contribute to the net variation of momentum.

This principle is represented in integral form by Equation 4:

$$\frac{\partial}{\partial t}\int_V \rho \boldsymbol{u}\,\mathrm{d}V = -\oint_{\partial V}\rho\,(\boldsymbol{u}\boldsymbol{u})\cdot\mathrm{d}\boldsymbol{A} - \oint_{\partial V} p\,\mathrm{d}\boldsymbol{A} + \oint_{\partial V}\boldsymbol{\tau}\cdot\mathrm{d}\boldsymbol{A} + \int_V \boldsymbol{F}\,\mathrm{d}V \tag{4}$$

where ρ represents the density of the fluid, $\boldsymbol{F}$ is the vector of external forces, p corresponds to the pressure, $\boldsymbol{u}$ is the velocity vector, $\boldsymbol{\tau}$ is the stress tensor and $\mathrm{d}\boldsymbol{A}$ is the area vector, oriented away from the control surface.

By applying the conservation of momentum principle and considering an incompressible fluid with constant viscosity, we obtain the Navier–Stokes equation:

$$\rho\frac{\mathrm{D}\boldsymbol{u}}{\mathrm{D}t} = -\nabla p + \mu\nabla^2\boldsymbol{u} + \boldsymbol{F}, \tag{5}$$

where ∇p represents the pressure gradient, $\mu\nabla^2\boldsymbol{u}$ the viscous term, and $\boldsymbol{F}$ the body forces. This formulation adopts the Newtonian fluid assumption, meaning that the viscous stress tensor is proportional to the rate-of-deformation tensor:

$$\boldsymbol{\tau} = \mu\left(\nabla\boldsymbol{u} + (\nabla\boldsymbol{u})^T\right).$$

The divergence of this tensor simplifies to the term $\mu\nabla^2\boldsymbol{u}$ due to the incompressibility constraint ($\nabla\cdot\boldsymbol{u} = 0$).

The momentum balance can also be expressed in the general form known as the Cauchy momentum equation:

$$\frac{\partial(\rho\mathbf{u})}{\partial t} + \nabla\cdot(\rho\,\mathbf{u}\mathbf{u}) = \nabla\cdot\boldsymbol{\sigma} + \mathbf{F}, \tag{6}$$

where $\boldsymbol{\sigma}$ is the Cauchy stress tensor, which incorporates both pressure and viscous contributions and represents the contact forces acting on the fluid. The definition of the Cauchy momentum equation will be useful later for recovering the macroscopic equations of fluid mechanics through the Boltzmann equation.

2.2 KINETIC THEORY OF GASES

The kinetic theory of gases provides the microscopic foundation for understanding the macroscopic behavior of fluids. At the molecular level, gases consist of an immense number of particles in constant chaotic motion. Attempting to determine the exact position and velocity of each particle over time in order to describe the fluid as a whole is an unfeasible task. Recognizing this, James Clerk Maxwell and Ludwig Boltzmann applied the principles of statistical mechanics to formulate a theory that

connects microscopic dynamics with macroscopic thermodynamic and hydrodynamic properties. Within this framework, the kinetic theory of gases not only explains the fundamental behavior of fluids but also establishes the basis for modern particle-based computational models, such as the LBM, which will be addressed in the following sections.

2.2.1 Distribution Function

The central quantity in kinetic theory is the particle distribution function $f(\boldsymbol{x}, \boldsymbol{\xi}, t)$ (Krüger *et al.*, 2017). While $\rho(\boldsymbol{x}, t)$ describes the macroscopic mass density at a given position $\boldsymbol{x}$ and time t, the distribution function provides a more detailed picture: it characterizes the density of particles not only in physical space but also in velocity space. In other words, $f(\boldsymbol{x}, \boldsymbol{\xi}, t)$ can be interpreted as the mass density of particles located at position $\boldsymbol{x} = (x, y, z)$ and moving with velocity $\boldsymbol{\xi} = (\xi_x, \xi_y, \xi_z)$ at time t.

From this microscopic perspective, macroscopic quantities such as density, momentum, and energy can be obtained as moments of the distribution function. For instance, the mass density is given by

$$\rho(\boldsymbol{x}, t) = \int f(\boldsymbol{x}, \boldsymbol{\xi}, t)\, d\boldsymbol{\xi} \,, \tag{7}$$

while the momentum density is expressed as

$$\rho(\boldsymbol{x}, t)\, \boldsymbol{u}(\boldsymbol{x}, t) = \int \boldsymbol{\xi}\, f(\boldsymbol{x}, \boldsymbol{\xi}, t)\, d\boldsymbol{\xi} \,, \tag{8}$$

where $\boldsymbol{u}(\boldsymbol{x}, t)$ denotes the macroscopic velocity field. Higher-order moments, such as those involving quadratic terms in $\boldsymbol{\xi}$, are associated with quantities like pressure and stress tensors.

The total energy density of the system can also be recovered from f. It is given by the second-order moment of the particle velocities:

$$\rho(\boldsymbol{x}, t)\, E(\boldsymbol{x}, t) = \frac{1}{2} \int |\boldsymbol{\xi}|^2\, f(\boldsymbol{x}, \boldsymbol{\xi}, t)\, d\boldsymbol{\xi} \,, \tag{9}$$

where $E(\boldsymbol{x}, t)$ is the total energy per unit mass, which includes both the macroscopic kinetic energy $\frac{1}{2}|\boldsymbol{u}|^2$ and the internal energy associated with the random thermal motion of the gas particles. To isolate the internal energy contribution, one introduces the concept of peculiar velocity, $\boldsymbol{v} = \boldsymbol{\xi} - \boldsymbol{u}$, which measures the deviation of the particle velocity from the local mean velocity, and substitutes it into Equation 9, leading to:

$$\rho(\boldsymbol{x}, t)\, e(\boldsymbol{x}, t) = \frac{1}{2} \int |\boldsymbol{v}|^2\, f(\boldsymbol{x}, \boldsymbol{\xi}, t)\, d\boldsymbol{\xi} \tag{10}$$

where e is the internal energy per unit mass.

Pressure can also be expressed as a moment of the distribution function. The most direct derivation comes from considering that particles impart momentum when colliding with a surface. Each collision transfers momentum normal to the surface, and the cumulative effect of these collisions per unit time and area defines the pressure.

As a shortcut, the same result can be reached via the equipartition theorem of classical statistical mechanics. Each degree of freedom (i.e. translation, vibration and rotation) contributes $\frac{1}{2}RT$ to the specific internal energy (Thompson, 1972), where R is the specific gas constant and T is the temperature. For monatomic gases, only translational motion exists, providing three degrees of freedom. Consequently, the internal energy per unit mass is

$$e = \frac{3}{2}RT \tag{11}$$

and, by the ideal gas law,

$$p = \rho RT \ . \tag{12}$$

Combining both relations leads to a direct connection between pressure and internal energy:

$$p = \frac{2}{3}\rho e = \frac{1}{3}\int |\boldsymbol{v}|^2 \, f(\boldsymbol{x}, \boldsymbol{\xi}, t) \, d\boldsymbol{\xi} \tag{13}$$

2.2.2 Equilibrium Distribution Function

When two particles collide at the microscopic level, their outgoing directions are highly sensitive to small variations in their initial relative positions. As a result, collisions tend to randomize these directions and progressively even out the angular distribution of particle velocities around the mean velocity $\boldsymbol{v}$. If the system is left undisturbed for a sufficient amount of time, this process leads the distribution function toward an equilibrium state, which becomes isotropic in velocity space centered around $\boldsymbol{\xi} = \boldsymbol{u}$.

For monoatomic particles this state of equilibrium can be described by the Boltzmann distribution function given by

$$f^{eq}(\boldsymbol{v}) = \left(\frac{m}{2\pi k_b T}\right)^{\frac{3}{2}} \exp\left(-\frac{m\,|\boldsymbol{v}|^2}{2k_b T}\right), \tag{14}$$

where k_b is the Boltzmann constant and $R = k_b/m$.

2.2.3 Maxwell-Boltzmann Equation

One may describe the system through the distribution function of its particles, but what is truly compelling is to understand how this system evolves over time. To bridge the gap between microscopic dynamics and macroscopic behavior, James Clerk

Maxwell and Ludwig Boltzmann formulated the foundational principles of statistical mechanics, introducing an equation that makes it possible to analyze the temporal evolution of distribution functions.

In this section, the standard index notation commonly used in kinetic theory will be adopted to express spatial and velocity derivatives in a compact form. For a detailed explanation of this notation, the reader is referred to Kundu *et al*. (2024), which provides an extended and accessible presentation of its foundations. This notation simplifies the representation of tensor contractions and will be employed throughout the remaining derivations.

The rate of change of the probability along the trajectory of a particle under the exclusive action of an external force is zero. However, when the particle can undergo collisions with other particles, this probability may change. The variation associated with collisions is represented by the collision operator, denoted by $\Omega(f)$. This leads to the following relation:

$$\frac{\mathrm{d}f}{\mathrm{d}t} = \frac{\partial f}{\partial t} + \frac{\partial f}{\partial x_\beta}\frac{\mathrm{d}x_\beta}{\mathrm{d}t} + \frac{\partial f}{\partial \xi_\beta}\frac{\mathrm{d}\xi_\beta}{\mathrm{d}t} = \Omega(f). \tag{15}$$

Looking at this equation, one observes that the term $\mathrm{d}x_\beta/\mathrm{d}t = \xi_\beta$, and from Newton's second law, the specific body force gives $\mathrm{d}\xi_\beta/\mathrm{d}t = F_\beta/\rho$. Substituting in Equation 15 gives:

$$\frac{\mathrm{d}f}{\mathrm{d}t} = \frac{\partial f}{\partial t} + \xi_\beta\frac{\partial f}{\partial x_\beta} + \frac{F_\beta}{\rho}\frac{\partial f}{\partial \xi_\beta} = \Omega(f)\ . \tag{16}$$

This equation can be regarded as a kind of advection equation: the first two terms represent the distribution functions advected with the velocity $\boldsymbol{\xi}$ of its particles. The third term accounts for the forces acting on this velocity. On the right-hand side, we have the source term, which represents the local redistribution of f due to collisions.

It is known that collisions conserve quantities of mass, momentum, and in the monoatomic case, translational energy. These conservation constraints can be represented as moments of the collision operator (Krüger *et al*., 2017).

$$\int \Omega(f)\ \mathrm{d}^3\xi = 0 \tag{17}$$

$$\int \xi\ \Omega(f)\ \mathrm{d}^3\xi = 0 \tag{18}$$

$$\int |\xi|^2\ \Omega(f)\ \mathrm{d}^3\xi = 0 \tag{19}$$

Any useful collision operator must both respect the conserved quantities as expressed and ensure that the distribution function f locally evolves towards its equilibrium f_{eq}.

2.2.4 Connection with Fluid Mechanics

The link with the macroscopic equations of fluid mechanics arises from taking moments of the Boltzmann equation (Equation 16), obtained by multiplying it by functions of $\boldsymbol{\xi}$ and integrating over the velocity space:

$$\Pi_0 = \int f \, \mathrm{d}^3\xi = \rho \, , \tag{20}$$

$$\Pi_\alpha = \int \xi_\alpha f \, \mathrm{d}^3\xi = \rho u_\alpha \, , \tag{21}$$

$$\Pi_{\alpha\beta} = \int \xi_\alpha \xi_\beta f \, \mathrm{d}^3\xi \, , \tag{22}$$

$$\Pi_{\alpha\beta\gamma} = \int \xi_\alpha \xi_\beta \xi_\gamma f \, \mathrm{d}^3\xi \, . \tag{23}$$

The first two moments yield the macroscopic fields of mass and momentum density. The second-order moment directly represents the momentum flux tensor according to the definition of the distribution function.

In order to incorporate force terms, it is necessary to evaluate the corresponding moments of the force term. This can be achieved by performing an integration by parts, as shown below:

$$\int \frac{\partial f}{\partial \xi_\beta} \, \mathrm{d}^3\xi = 0, \tag{24}$$

$$\int \xi_\alpha \, \frac{\partial f}{\partial \xi_\beta} \, \mathrm{d}^3\xi = -\int \frac{\partial \xi_\alpha}{\partial \xi_\beta} f \, \mathrm{d}^3\xi = -\rho\delta_{\alpha\beta}, \tag{25}$$

$$\int \xi_\alpha \xi_\alpha \frac{\partial f}{\partial \xi_\beta} \, \mathrm{d}^3\xi = -\int \frac{\partial (\xi_\alpha \xi_\alpha)}{\partial \xi_\beta} f \, \mathrm{d}^3\xi = -2\rho u_\beta. \tag{26}$$

Integrating the Boltzmann equation (Equation 16) over the velocity space allows us to derive the mass conservation equation:

$$\frac{\partial}{\partial t} \int f \, \mathrm{d}^3\xi + \int \xi_\beta \frac{\partial f}{\partial x_\beta} \, \mathrm{d}^3\xi + \frac{F_\beta}{\rho} \int \frac{\partial f}{\partial \xi_\beta} \, \mathrm{d}^3\xi = \int \Omega(f) \, \mathrm{d}^3\xi. \tag{27}$$

After substituting Equations 17, 20, 21, and 24, the differential form of the mass conservation equation is obtained, which corresponds to the well-known continuity equation:

$$\frac{\partial \rho}{\partial t} + \frac{\partial (\rho u_\beta)}{\partial x_\beta} = 0 \ . \tag{28}$$

This relation expresses the local conservation of mass, where the rate of density change in time is balanced by the divergence of the mass flux.

To obtain the momentum conservation law, one considers the first moment of the Boltzmann equation. By multiplying the equation by ξ_α and integrating over the velocity space, the following expression is derived:

$$\frac{\partial (\rho u_\alpha)}{\partial t} + \frac{\partial \Pi_{\alpha\beta}}{\partial x_\beta} = F_\alpha \ . \tag{29}$$

This equation corresponds to the balance of linear momentum, where the temporal variation of momentum density and the divergence of the flux tensor are driven by the external force term F_α.

Extending this procedure to the second moment of the Boltzmann equation allows us to obtain the energy conservation relation. In this case, the equation reads:

$$\frac{\partial (\rho E)}{\partial t} + \frac{1}{2}\frac{\partial \Pi_{\alpha\alpha\beta}}{\partial x_\beta} = F_\beta u_\beta \ . \tag{30}$$

Here, the temporal evolution of the energy density ρE is linked to the transport of higher-order fluxes and the work performed by external forces.

The ability to recover the governing equations of fluid mechanics from the kinetic theory of gases, under appropriate assumptions, demonstrates the consistency of the formalism and reinforces its validity. This approach establishes the connection between the microscopic description and the macroscopic conservation laws. A more detailed account of the derivations presented above can be found in He and Luo (1997).

2.3 LATTICE BOLTZMANN METHOD (LBM)

The governing equations of fluid mechanics are notoriously difficult to solve in the general case. While specific configurations, such as Couette or Poiseuille flow, admit analytical solutions, most practical problems require numerical treatment.

From the previous sections, we have seen that macroscopic fluid properties can be recovered through a mesoscopic analysis of the Boltzmann equation. However, obtaining an analytical solution is a complex challenge, since its fundamental quantity—the distribution function—depends on seven variables: x, y, z, ξ_x, ξ_y, ξ_z and t. Paradoxically, when discretized in a particular manner, the Boltzmann equation becomes a numerical method of simple implementation and high scalability.

2.3.1 Fundamentals of LBM

The LBM relies on a kinetic description of fluid motion in which the state of the system is represented by particle distribution functions evolving on a discrete lattice. To introduce the dynamics of the method, the discrete evolution of these particle populations is first expressed by the Lattice Boltzmann Equation, obtained from the discretization of the kinetic formulation in velocity space, physical space, and time:

$$f_i(\boldsymbol{x} + \boldsymbol{c}_i\Delta t, t + \Delta t) = f_i(\boldsymbol{x}, t) + \Omega_i(\boldsymbol{x}, t), \tag{31}$$

which shows that the evolution of the distribution function f_i in the lattice is governed by the collision process Ω_i occurring locally.

Although different collision operators such as BGK, TRT, and MRT are available in the literature and will be discussed separately later, they all share the fundamental idea that the particle populations relax toward an equilibrium state. This equilibrium is obtained from the Hermite expansion of the Maxwell–Boltzmann distribution, leading to the expression:

$$f_i^{eq}(\boldsymbol{x}, t) = w_i\rho\left(1 + \frac{\boldsymbol{u}\cdot\boldsymbol{c}_i}{c_s^2} + \frac{(\boldsymbol{u}\cdot\boldsymbol{c}_i)^2}{2c_s^4} - \frac{\boldsymbol{u}\cdot\boldsymbol{u}}{2c_s^2}\right). \tag{32}$$

With the equilibrium distribution defined, the connection to macroscopic quantities becomes clear. In the LBM, the fundamental quantity is the *discrete-velocity distribution function* $f_i(\boldsymbol{x}, t)$, also referred to as the *particle population*. Although analogous to the continuous distribution function from kinetic theory, here both the position $\boldsymbol{x}$ and the discrete velocities $\boldsymbol{c}_i$ lie on a regular lattice with spacing Δx and timestep Δt. From these populations, the macroscopic fields are obtained through the standard kinetic moments:

$$\rho(\boldsymbol{x}, t) = \sum_i f_i(\boldsymbol{x}, t) \quad \text{and} \quad \rho\boldsymbol{u}(\boldsymbol{x}, t) = \sum_i \boldsymbol{c}_i f_i(\boldsymbol{x}, t). \tag{33}$$

The key distinction is that the distribution function is no longer continuous but defined over a finite set of velocity directions, representing a fundamental shift from classical formulations. This structure sets the LBM apart from conventional CFD methods not because space and time are represented on a grid—an aspect shared with

finite-difference, finite-volume, and finite-element approaches—but because the range of admissible particle velocities is restricted to a prescribed set.

The construction of the velocity set can follow different strategies. A common convention is the notation DdQq, where d denotes the number of spatial dimensions and q the number of discrete velocities; widely used examples in the literature include D1Q3, D2Q9, D3Q15, D3Q19, and D3Q27 (Figure 2). Although enlarging this set generally enhances the ability to capture more physical behavior, it also increases the associated memory cost.

Figure 2 – Velocity sets example — D2Q9 and D3Q15

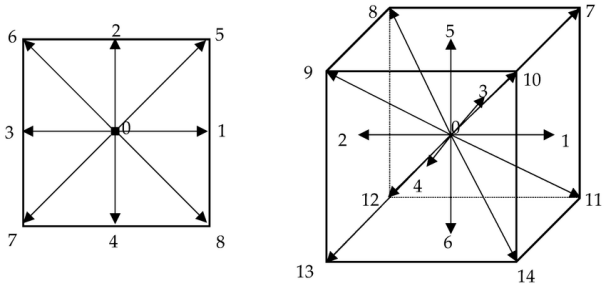

Source: Chen *et al.* (2017, p. 3).

In addition to defining the velocity directions, each set is associated with a specific collection of weights w_i, which determine the relative contribution of each velocity to the macroscopic variables (Table 1). These weights arise from the lattice representation of the Maxwell–Boltzmann equilibrium distribution and are chosen so that the discrete model reproduces the correct hydrodynamic moments up to second order.

Table 1 – Velocities and weights of the D2Q9 model

i	0	1	2	3	4	5	6	7	8
w_i	$\frac{4}{9}$	$\frac{1}{9}$	$\frac{1}{9}$	$\frac{1}{9}$	$\frac{1}{9}$	$\frac{1}{36}$	$\frac{1}{36}$	$\frac{1}{36}$	$\frac{1}{36}$
c_{ix}	0	1	0	-1	0	1	-1	-1	1
c_{iy}	0	0	1	0	-1	1	1	-1	-1

Source: Krüger *et al.* (2017, p. 88).

Another interesting characteristic of the LBM is that the time step Δt and the lattice spacing Δx representing the temporal and spatial resolution of the simulation can be chosen as any system of units. Although one may employ SI or Imperial units, the lattice unit system is most commonly adopted because it sets both $\Delta t = 1$ and $\Delta x = 1$, which simplifies operations in lattice space while still allowing conversion back to physical units through the nondimensional parameters of the problem. This guarantees that physical behavior is consistently reproduced across different scales, provided that the relevant dimensionless numbers, such as the Reynolds number, are properly matched.

In view of the previous discussion, the LBM is structured into two elementary steps: *collision* and *streaming*. As noted earlier, the particle distribution functions f_i at each lattice node interact and relax toward equilibrium, modeling the effect of microscopic collisions, while the specific form of this relaxation is determined by the chosen collision operator, which strongly influences the accuracy, stability, and computational cost of the method.

The collision step is followed by the streaming step, in which the post-collision distributions f_i^* are advected along the discrete velocity directions $\mathbf{c}_i$ defined by the lattice, as expressed by

$$f_i(\mathbf{x} + \mathbf{c}_i \Delta t, t + \Delta t) = f_i^*(\mathbf{x}, t) \ . \tag{34}$$

This transport corresponds to the propagation of the distribution functions from the current node to the neighboring nodes in the direction of $\mathbf{c}_i$, establishing communication between lattice sites (Figure 3) and enabling the temporal evolution of the flow field.

Figure 3 – Collision-Streaming Process

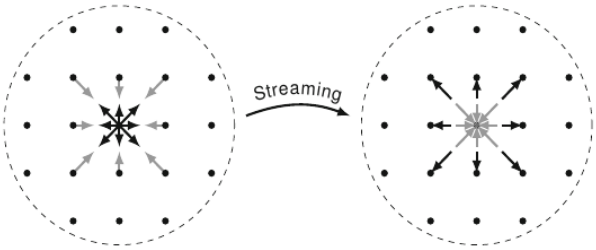

Source: Krüger *et al.* (2017, p. 65).

After the streaming process, it is necessary to impose the boundary conditions of the problem, as the accuracy of the method depends on their proper treatment, ensuring that the physical constraints at the domain boundaries are correctly enforced. Since these constraints play a central role in this work, the boundary conditions adopted will be discussed in detail in a later section.

2.3.2 Collision operators: BGK, TRT, MRT

In the LBM, the dynamics of the particle distributions are controlled by the collision operator, which defines how the distribution functions f_i relax towards their equilibrium values f_i^{eq}. The choice of collision operator directly affects the stability, accuracy, and computational cost of the simulation. The most commonly used operators are BGK, TRT, and MRT.

2.3.2.1 BGK Operator (Single Relaxation Time)

The BGK operator is the simplest and is also known as the *single relaxation time* model (Bhatnagar *et al.*, 1954; Qian *et al.*, 1992). It is defined as

$$\Omega^{BGK} = -\frac{1}{\tau}\left(f - f^{eq}\right), \tag{35}$$

where τ is the relaxation time, and the kinematic viscosity of the fluid is related to τ by

$$\nu = c_s^2\left(\tau - \frac{1}{2}\right)\Delta t, \tag{36}$$

with c_s being the lattice speed of sound.

This model replaces the full collision operator with a linear relaxation toward an equilibrium, thereby eliminating the statistical noise inherent from older LBM approaches such as lattice gas automata (Qian *et al.*, 1992). The equilibrium distribution is truncated at second order in the macroscopic velocity, ensuring the required isotropy to recover the incompressible Navier–Stokes equations through a Chapman–Enskog expansion.

Although structurally simple, this operator enforces a single relaxation time for all kinetic modes, which tightly couples viscosity, stability, and dissipation. This constraint limits the robustness of the method in flows with strong gradients or very low viscosities, where high sensitivity to the choice of τ may lead to numerical instabilities.

2.3.2.2 TRT Operator (Two Relaxation Time)

The TRT operator offers a compromise between the simplicity of BGK and the robustness of MRT. In this model, all moments related to even-order polynomials in velocity are relaxed with a rate ω^+, and the odd-order moments with ω^- (Ginzburg *et al.*, 2008). These relaxation rates follow the standard LBM definition $\omega = 1/\tau$, with τ being the relaxation time. The particle distributions are decomposed into symmetric and antisymmetric parts:

$$f_i^{\pm} = \frac{1}{2}\left(f_i \pm f_{\bar{i}}\right), \tag{37}$$

where $f_{\bar{i}}$ is the distribution in the opposite lattice direction of f_i. Each component relaxes towards equilibrium with a distinct relaxation time:

$$f_i\left(\boldsymbol{x} + \boldsymbol{c}_i\Delta t, t + \Delta t\right) = f_i - \omega^+\Delta t\left(f_i^+ - f_i^{eq+}\right) - \omega^-\Delta t\left(f_i^- - f_i^{eq-}\right). \tag{38}$$

By appropriately choosing the relaxation parameters ω^+ and ω^-, the TRT model achieves improved stability compared to the BGK model while remaining computationally efficient. The TRT model recovers the Navier-Stokes equations with the kinematic shear viscosity given by:

$$\nu = c_s^2 \left(\frac{1}{\omega^+} - \frac{1}{2} \right) \Delta t. \tag{39}$$

Even though the TRT formulation employs two relaxation parameters, the viscosity depends solely on ω^+, so the expression above is identical to the BGK viscosity when $\omega^+ = \omega$. This means that both schemes yield the same macroscopic viscous behavior, and the improved stability of the TRT operator comes entirely from the independent control of the odd kinetic modes through ω^-.

While ω^- may appear to be a free parameter, Ginzburg *et al*. (2008) introduces the so-called *magic parameter* Λ, which characterizes the truncation error and stability properties of the scheme. This parameter is defined as:

$$\Lambda = \left(\frac{1}{\omega^+ \Delta t} - \frac{1}{2} \right) \left(\frac{1}{\omega^- \Delta t} - \frac{1}{2} \right). \tag{40}$$

By choosing an appropriate value of Λ, one fixes the odd-order relaxation rate ω^- and controls important numerical properties of the TRT scheme. Common choices found in the literature include (Ginzburg *et al*., 2008):

- $\Lambda = 1/12$ cancels the third–order spatial error, leading to optimal accuracy for pure advection problems.
- $\Lambda = 1/6$ cancels the fourth–order spatial error, providing the most accurate results for pure diffusion equations.
- $\Lambda = 3/16$ places the effective bounce–back boundary exactly halfway between wall and fluid nodes, producing correct Poiseuille flow profiles.
- $\Lambda = 1/4$ yields the most stable simulations, making it a robust default choice for general applications(Ginzburg *et al*., 2010).

2.3.2.3 MRT Operator (Multiple Relaxation Time)

The MRT operator improves upon the BGK and TRT model by allowing different relaxation rates for different moments (d'Humières, 1992; d'Humières, 2002). In this formulation, all distribution functions f_i are assembled into a vector $\vec{f}$ whose components represent the particle populations associated with each discrete lattice velocity. To isolate the main kinetic contributions, the vector of distributions is transformed into a vector of moments $\vec{m}$, whose entries are linear combinations of the f_i.

Working in moment space is advantageous because each moment corresponds to a specific kinetic mode. The conserved moments, density and momentum, must not change during the collision step, while the higher-order non-conserved moments can be damped at different rates to control numerical dissipation. This separation allows the MRT operator to assign distinct relaxation rates to individual moments.

In this way, the collision step is performed in the moment space, obtained by

$$\vec{m} = M\vec{f}, \tag{41}$$

where M is the transformation matrix whose rows define the linear combinations that map particle populations. The collision operator is then written as

$$\Omega^{MRT} = -M^{-1}SM\left(\vec{f} - \vec{f}^{eq}\right), \tag{42}$$

with S being a diagonal matrix containing the relaxation rates for each moment.

The main idea of the MRT model is to relax each moment individually through the matrix $\boldsymbol{S}$, and then transformed back to population space, where the streaming process occurs normally.

This model provides better numerical stability and accuracy by enabling independent tuning of the kinetic components that govern physical transport and those responsible for numerical dissipation. This makes it particularly suitable for high Reynolds number flows, complex geometries, and cases where accuracy and robustness are critical, at the cost of higher computational effort.

2.3.3 Boundary Conditions

Boundary conditions are required to properly constrain the solution of a fluid-flow problem and ensure that the computed fields remain mathematically well posed and physically meaningful. Without them, the system would admit multiple or undefined solutions, preventing a stable and consistent description of the flow. In the LBM, the same care is necessary when prescribing initial and boundary information. Defining a boundary condition consists of assigning specific values to the distribution functions $f_i(x,t)$ at the boundary nodes. Several boundary schemes have been developed for this purpose, with the most commonly used being the bounce–back rule, prescribed-velocity boundaries, and periodic conditions. The following subsections describe the bounce-back method used to treat solid boundaries and the momentum exchange approach (MEA) used to compute the forces acting on the obstacle. The inlet and outlet boundary conditions will be discussed later in the methodology section.

2.3.3.1 Zou and He (1997)

The inlet boundary condition with prescribed velocity in the LBM was formalized by Zou and He (1997), who proposed a procedure based on the bounce-back of the non-equilibrium part of the particle distributions. The method relies on the fact that, after the streaming step, certain incoming populations are unknown and must be reconstructed using the conservation equations together with an additional relation obtained by reflecting the non-equilibrium component. The computation is performed by

imposing the desired velocity at the boundary while determining the local density as part of the solution.

In the two-dimensional D2Q9 case shown in Fig. 2, assuming a vertical inlet boundary (for example, on the left side of the domain), the streaming step leaves the populations f_2, f_3, f_4, f_6, f_7 known. Given prescribed velocity components $(u_x, u_y = 0)$, the macroscopic definitions

$$\rho = \sum_i f_i \tag{43}$$

and

$$\rho \boldsymbol{u} = \sum_i f_i \boldsymbol{c}_i \tag{44}$$

are used to construct the system involving the unknown distributions f_1, f_5, f_8. Applying mass and momentum conservation yields

$$f_1 + f_5 + f_8 = \rho - (f_0 + f_2 + f_3 + f_4 + f_6 + f_7), \tag{45}$$

the x-momentum equation gives

$$f_1 + f_5 + f_8 = \rho u_{in} + (f_3 + f_6 + f_7), \tag{46}$$

and the y-momentum equation gives

$$f_5 - f_8 = -f_2 + f_4 - f_6 + f_7. \tag{47}$$

Consistency between Equation 45 and 46 provides the density at the inlet,

$$\rho = \frac{f_0 + f_2 + f_4 + 2(f_3 + f_6 + f_7)}{1 - u_{in}}, \tag{48}$$

when the velocity is prescribed. For the case of prescribed density, the velocity becomes the unknown and is obtained from the same equations with reversed roles. In both formulations, the remaining distributions are evaluated by enforcing bounce-back of the non-equilibrium part, namely,

$$f_1 - f_1^{eq} = f_3 - f_3^{eq}, \tag{49}$$

for opposite velocity directions normal to the boundary, which closes the system.

Using this additional relation, the unknown distributions take the explicit form

$$f_1 = f_3 + \frac{2}{3}\rho_{\text{in}} u_x, \tag{50}$$

$$f_5 = f_7 + \frac{1}{2}(f_2 - f_4) + \frac{1}{6}\rho_{\text{in}} u_x, \tag{51}$$

$$f_8 = f_6 + \frac{1}{2}(f_2 - f_4) + \frac{1}{6}\rho_{\text{in}} u_x, \tag{52}$$

which correspond to the reconstructed inlet populations consistent with the imposed kinematics and the reflected non-equilibrium state.

2.3.3.2 Breuer *et al*. (2000)

In the LBM simulations of Breuer *et al*. (2000), the inlet boundary condition was defined to reproduce a fully developed laminar channel flow upstream of the square cylinder, enforcing a parabolic velocity profile with a prescribed maximum velocity $u_{\max}$. This analytical Poiseuille profile was imposed at the left boundary of the channel.

Figure 4 – Breuer *et al*. (2000) inlet condition

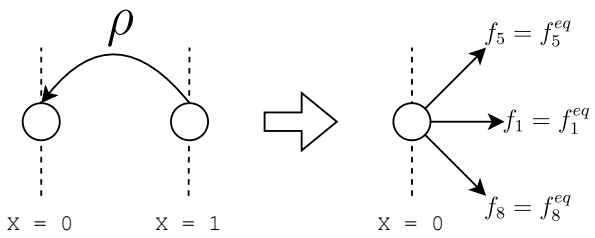

Source: Author (2025).

As illustrated in Figure 4, to implement this inflow condition in the LBM framework, the authors computed the equilibrium distribution at the inlet using the desired velocity field and a density extrapolated from inside the domain. Because only equilibrium distributions were applied, the authors extended the inlet length to guarantee that the slight non-equilibrium error introduced at the boundary vanished before reaching the cylinder.

2.3.3.3 Bounce-Back Method

The bounce-back condition is based on the principle that, when particle distributions propagate toward a solid boundary, they are reflected back to the site from which they originated (Figure 5). This approach implies that particles do not penetrate the solid barrier and enforces the no-slip condition at the wall.

Figure 5 – Schematic for the Bounce-Back boundary condition.

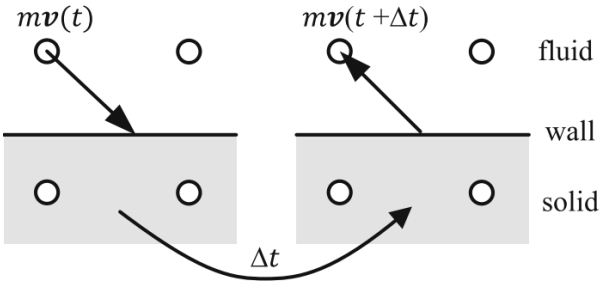

Source: Krüger *et al*. (2017, p. 176).

Populations leaving a given lattice node are reflected with the same magnitude and direction of velocity but with opposite orientation, following $\mathbf{c}_{\bar{i}} = -\mathbf{c}_i$, and they return to the original node at time $t + \Delta t$. This process is expressed mathematically by:

$$f_{\bar{i}}(\mathbf{x}, t + \Delta t) = f_i^*(\mathbf{x}, t) \tag{53}$$

where f_i^* is the distribution post-collision.

Following this idea, two commonly used formulations of the bounce-back scheme are the halfway and fullway. In the halfway model (Figure 6b), particle distributions are assumed to reach the wall halfway through a time step, so after streaming the reflected population returns directly to the lattice node from which it departed. In the fullway model (Figure 6a), the particle distributions are assumed to require an entire time step to reach the boundary before being reflected.

Figure 6 – Schematic for the Fullway (a) and Halfway (b) Bounce-back.

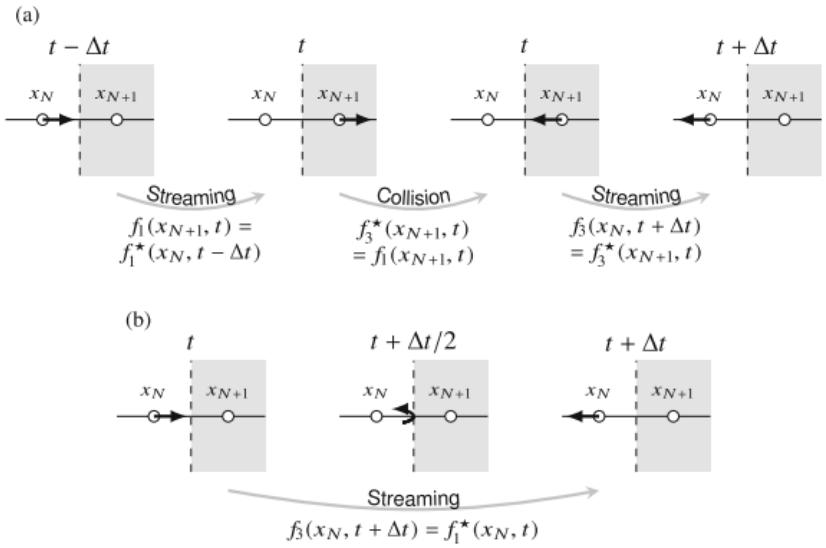

Source: Krüger *et al.* (2017, p. 177).

This work adopts the halfway scheme because it is simpler to implement and provides second-order accuracy at the solid wall. In contrast, the fullway formulation achieves only first-order accuracy, making the halfway model a more accurate choice for representing solid boundaries and enforcing the no-slip condition within the LBM framework

2.3.3.4 Force Calculation Method

The force acting on the obstacle is evaluated using the Momentum Exchange Method (MEM). In this approach, the interaction between fluid particles and the solid boundary is computed during the streaming step of the Lattice Boltzmann Method. Each time a distribution function f_i moving in direction $\mathbf{c}_i$ is reflected at a solid node, the associated momentum is exchanged between the fluid and the surface (Ladd, 1994).

The total momentum exchange can be expressed as

$$\Delta \boldsymbol{P} = \sum_{\vec{x}\epsilon S} \sum_{i\epsilon Q} 2 f_i(\vec{x}) \boldsymbol{c}_i \ , \tag{54}$$

where S denotes the set of nodes located at the boundary surface, Q is the number of discrete velocities associated with the chosen velocity set (e.g., $Q = 9$ for D2Q9 and $Q = 19$ for D3Q19). Here, f_i is the incoming distribution from the neighboring fluid node in direction i, and c_i is the corresponding discrete velocity for that direction.

If it is assumed that the momentum is exchanged smoothly during one time step Δt, one can easily find the force acting on the boundary:

$$\boldsymbol{F} = \frac{\Delta \boldsymbol{P}}{\Delta t}. \tag{55}$$

From the force components, drag and lift coefficients can be computed as

$$C_d = \frac{F_x}{\frac{1}{2}\,\rho\, U^2\, D}, \qquad C_l = \frac{F_y}{\frac{1}{2}\,\rho\, U^2\, D}, \tag{56}$$

where F_x and F_y are the streamwise and transverse force components, ρ the fluid density, U the reference velocity, and D the characteristic length (the side of the square cylinder).

Chapman–Enskog analysis shows that the method achieves second-order accuracy in space and time when combined with the bounce-back boundary condition. This means that the discretization error in the force calculation decreases proportionally to Δx^2 and Δt^2. As a result, the MEM is computationally simple while still providing reliable and accurate force predictions in LBM simulations.

2.4 FLOW AROUND OBSTACLES AND VORTEX FORMATION

Understanding how the flow behaves around immersed bodies is essential for analyzing the resulting physical processes. Given that the main focus of this work is the square obstacle, this section presents literature findings that examine how the Reynolds number influences different flow regimes.

The flow around bluff bodies, such as square cylinders, exhibits a variety of hydrodynamic regimes that are strongly dependent on the Reynolds number. At very low Reynolds numbers ($Re < 1$), the flow is dominated by viscous forces, characterizing the so-called *creeping flow*, where no boundary layer separation occurs, as shown in Figure 7.

As Re increases, the flow begins to separate at the trailing edges of the cylinder, giving rise to a steady recirculation region composed of two symmetric vortices behind the obstacle, as shown in Figure 8.

Figure 7 – Creeping Flow at $Re = 1$

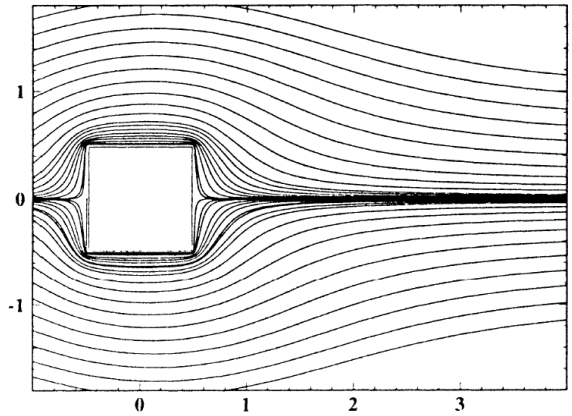

Source: Breuer *et al.* (2000, p. 190).

Figure 8 – Recirculation region at $Re = 30$

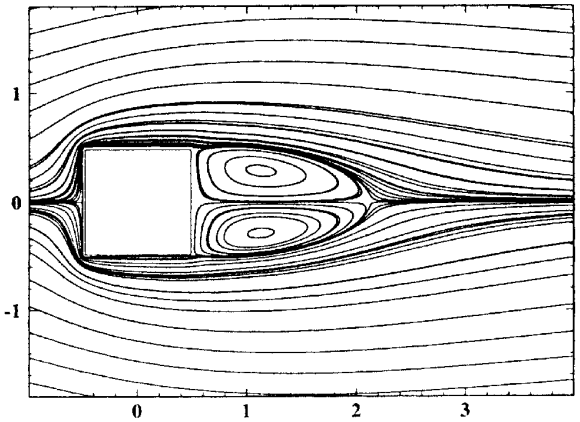

Source: Breuer *et al.* (2000, p. 190).

The length of this recirculation region grows linearly with Re, a behavior similar to that observed for circular cylinders, but with particularities due to the corners of the square body. According to Breuer *et al.* (2000), for Reynolds numbers in the range $5 < Re < 60$, the recirculation length is given by the empirical relation calculated by as

$$\frac{L_r}{D} = -0.065 + 0.0554\, Re, \tag{57}$$

where L_r is the recirculation length and D the cylinder diameter.

When the Reynolds number reaches critical values ($Re \approx 60$), the recirculation region becomes unstable, and periodic vortex shedding occurs, forming the well-known von Kármán vortex street, as shown in Figure 9.

At this stage, transverse oscillations start at the end of the near-wake and propagate downstream, generating an alternating periodic vortex pattern. The shedding wavelength decreases with increasing Re, intensifying the oscillation frequency.

Figure 9 – Von Kármán Vortex Street at $Re = 60$

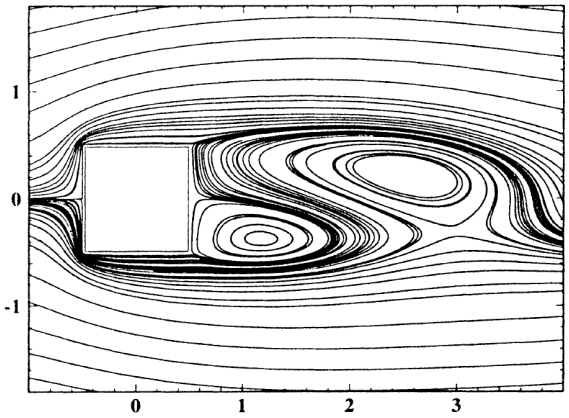

Source: Breuer *et al.* (2000, p. 190).

For higher values ($Re \approx 100 - 200$), flow separation already occurs at the leading edges of the square cylinder, significantly changing the wake dynamics and a clear von Kármán vortex street forms in a laminar regime.

Figure 10 – Von Kármán Vortex Street at $Re = 200$

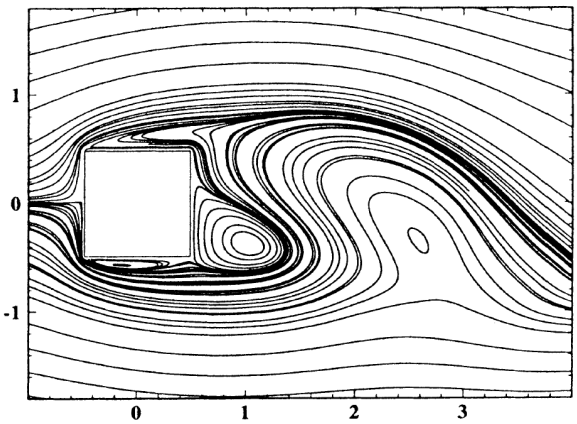

Source: Breuer *et al.* (2000, p. 190).

At $Re > 300$, although two-dimensional results are still attainable, the literature indicates that three-dimensional structures start to appear, leading to the transition to turbulence in the free shear layers.

Dimensionless parameters such as the drag coefficient (C_d), the recirculation length (L_r), and the Strouhal number (St) are widely used to characterize these regimes, and at low Re the coefficient C_d varies strongly because it reflects the balance between viscous and pressure forces. The recirculation length increases roughly linearly with Re, while the Strouhal number rises until a maximum near $Re \approx 150$ and then decreases toward nearly constant values, a behavior linked to the shift of the separation point that modifies the shedding frequency.

3 METHODOLOGY

The present work was conducted through an approach aimed at studying the influence of boundary conditions and collision models on the flow around a bluff body in Lattice Boltzmann simulations. This approach can be outlined in three main stages: a review of the literature , the implementation of a simulation code, the validation of the developed code and the comparison with recent studies.

In the literature review, the primary objective was to identify previous studies in which the method was applied to flows in closed channels and in domains with obstacles. Alongside numerical investigations, experimental works conducted under conditions comparable to those in recent studies were also examined. This dual perspective provides means to validate and evaluate the simulations. During the review, however, a noticeable gap was identified regarding the assessment of boundary conditions and their influence on the accurate representation of flow phenomena.

Subsequently, a custom code was developed in C++ to simulate the case under investigation, designed to facilitate the testing of different boundary conditions and collision operators. Computational resources and technical support for running the simulations were provided by the Laboratory of Scientific Computing (LabCC) at the Federal University of Santa Catarina, where the executions were performed on its high-performance computing cluster.

Finally, the code was validated against a plane Poiseuille flow benchmark over a range of grid resolutions, Reynolds numbers, and boundary conditions. Building upon it, the study reproduced the results of Wang *et al*. (2015) and systematically varied the outlet boundary conditions, allowing the identification of the configuration that best replicates the available experimental data from Reyes *et al*. (2013).

3.1 STATE OF THE ART

Flow around bluff bodies is an important problem in fluid dynamics due to its relevance in aeronautics, civil engineering, and geophysical applications. The unsteady wakes behind simple obstacles such as squares, cylinders or spheres serve as canonical models for more complex flows. Among the main features are the onset of vortex shedding, its transition to three-dimensionality, and the emergence of secondary instabilities, which are critical for understanding force fluctuations, noise generation, and flow-induced vibrations.

Early work by Kármán (1911) established the theoretical basis for the vortex street mechanism behind bluff bodies, describing the periodic shedding of vortices in the wake of a cylinder. Later, Homann (1936) investigated the phenomena responsible

for erroneous Pitot tube readings in viscous flows. The study combined experiments and theoretical analysis, providing some of the first systematic data on pressure and velocity distributions around cylinders, which contributed to the early understanding of bluff-body aerodynamics.

Building on this foundation, Shair *et al*. (1963) showed experimentally that the stability of the laminar wake behind a circular cylinder is strongly influenced by confinement. Their results emphasized the role of blockage effects in interpreting laboratory measurements of vortex shedding and transition. In parallel, other researchers such as Vickery (1966) and Nakaguchi *et al*. (1968) extended investigations to rectangular cylinders.

Later, Bearman and Trueman (1972), Okajima (1982), Bearman and Obasaju (1982), provided experimental studies of rectangular-cylinder wakes. Bearman and Trueman (1972) examined the effect of depth-to-width ratio d/h on drag, base pressure, and Strouhal number. Bearman and Obasaju (1982) extended this by measuring pressure fluctuations in square cylinders, both fixed and oscillating. They showed that in the lock-in regime the vortex shedding frequency synchronizes with the body motion, altering surface pressures and reducing mean drag, with two shedding modes observed: one natural and another tied to the oscillation frequency. In parallel, Okajima (1982) mapped Strouhal numbers for rectangular cylinders over a wide range of Reynolds numbers using water channels for low Reynolds and wind tunnels for higher Reynolds, identifying discontinuities and two distinct regimes depending on whether the flow reattached on the sides or not.

Davis *et al*. (1984) combined experiments and two-dimensional simulations, showing the influence of blockage ratio on vortex shedding. Mukhopadhyay *et al*. (1992) extended this with a systematic numerical study, demonstrating that confinement damps wake periodicity downstream, reestablishing a parabolic profile and linking unconfined and confined regimes. Suzuki *et al*. (1993) reported a “crisscross” vortex motion across the channel centerline, absent in unconfined wakes, further stressing the role of blockage. With increasing computational resources, Breuer *et al*. (2000) achieved high-fidelity simulations in good agreement with experiments, while Turki *et al*. (2003) analyzed different blockage ratios, showing their effect on the onset of shedding, force coefficients, and wake symmetry. Together, these contributions established how geometry, Reynolds number, and confinement govern rectangular-cylinder wakes.

More recently, the LBM has been applied to this problem. Wang *et al*. (2015) performed two-dimensional LBM simulations of square cylinders in a channel, analyzing Reynolds and collision operators. Their computations reproduced lift and drag coefficients, confirming that LBM captures the primary shedding mechanism. However, no experimental data was found in the literature for confined square cylinders in the Reynolds range considered by Wang, which limits direct validation of their re-

sults. They also reported that the method could not reproduce the secondary oscillation modes observed numerically by Breuer *et al*. (2000) using FVM, highlighting a possible limitation of standard LBM models. While Okajima (1982) conducted experiments within the same Reynolds number range but on unconfined cylinders, Bearman and Obasaju (1982) focused on different blockage ratios but at Reynolds numbers outside the range considered by Wang *et al*. (2015), thus preventing a direct comparison with their numerical results.

In contrast, Reyes *et al*. (2013) provided experimental data for confined three-dimensional laminar flow past a square prism with a high blockage ratio (1/2.5) and aspect ratio 1, observing that lateral walls significantly affect the flow. They found that confinement delays the onset of vortex shedding to $Re \approx 170$, compared to $Re \approx 60$ for unconfined cases, and that the transition from steady to unsteady flow occurs gradually through a pulsating recirculation regime. Although the geometry and dimensionality differ from the two-dimensional setup of Wang *et al*. (2015), the experimental results of Reyes *et al*. (2013) were used in the present work as a reference for comparison with the numerical simulations in confined configurations.

In conclusion, the present work builds on these studies as part of a broader incremental effort to apply the LBM to progressively more complex problems in aerospace applications. With this motivation, a square cylinder was selected to avoid geometric uncertainties associated with curved surfaces and to rely on a configuration that has been extensively studied experimentally, providing an excellent benchmark for analyzing inlet and outlet boundary conditions. Additionally, the work of Wang *et al*. (2015) highlights the occurrence of secondary oscillation modes, which makes this phenomenon particularly relevant to investigate in the context of confined flows.

3.2 SIMULATION SETUP

The numerical configuration adopted in this work follows the setup used by Wang *et al*. (2015). The flow was simulated using the D2Q9 lattice model with BGK, MRT, and TRT collision operators. A square cylinder with side length $D = 40$ was positioned along the channel centerline, as illustrated in Figure 11.

Figure 11 – Schematic of the flow past a square cylinder in a 2D channel

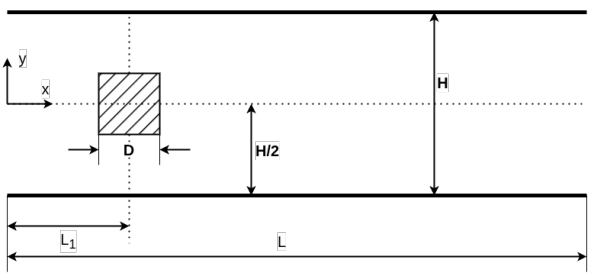

Source: Adapted from Wang *et al*. (2015, p. 669).

The computational domain was defined with overall dimensions $L \times H$, where $L = 50D$ and $H = 8D$, with the cylinder centered at a distance $L_1 = 12.5D$ from the inlet. The blockage ratio, defined as the ratio between the cube side length and the channel height, was set to $1/8$, and for comparison with the experimental study of Reyes *et al*. (2013), the domain height was adjusted to match the corresponding blockage ratio reported by the authors.

At the inlet, a parabolic velocity profile with a maximum velocity of $0.1c_s$ (ten percent of the speed of sound) was imposed to ensure incompressible flow, following the boundary condition proposed by Breuer *et al*. (2000).

On the surfaces of the obstacle and channel walls, the half-way bounce-back boundary condition was applied, ensuring second-order accuracy in the representation of no-slip solid boundaries. As illustrated in Figure 12, this condition operates by reflecting the distribution functions into their opposite lattice directions during the streaming step.

Figure 12 – Halfway Bounce-back Scheme

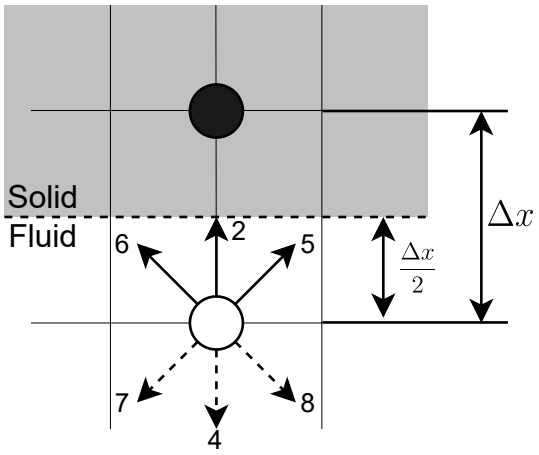

Source: Author (2025).

At the outlet, four different approaches were tested—convective, null-derivative, first order extrapolation and second order extrapolation conditions—in order to identify the most suitable strategy for visualizing the secondary vortex shedding modes.

The relaxation parameter τ was obtained as

$$\tau = 3\nu + 0.5, \tag{58}$$

where the kinematic viscosity ν is defined by

$$\nu = \frac{U_{\max} D}{Re}, \tag{59}$$

with $U_{\max}$ representing the maximum inlet velocity, D the cube side used as the characteristic length, and Re the corresponding Reynolds number. This formulation allowed

the analysis of cases within the range $60 \leq Re \leq 300$, covering the transition from initial vortex formation to the emergence of secondary modes reported in FVM studies.

The analysis of results focused on the characterization of vortices by calculating the lift coefficient over time, which was then subjected to spectral analysis using the Fast Fourier Transform (FFT) to identify the dominant frequencies. The Power Spectral Density (PSD) was used to represent the energy distribution of the signal as a function of frequency, allowing identification of the vortex shedding modes. The Strouhal number, defined as

$$St = \frac{f_p D}{U_{\max}}, \tag{60}$$

where f_p denotes the dominant vortex shedding frequency, was employed as a dimensionless parameter to characterize the flow and to enable consistent comparison between different boundary conditions and reference data.

The code was validated using a benchmark plane Poiseuille flow, where the L2 error norm was evaluated for all boundary conditions considered, as defined in Eq. (69). Following this validation, a comparison with the results presented by Wang *et al*. (2015) was conducted to assess whether the data obtained by the code were consistent with their findings. Since no experimental data under the same conditions as the present simulations are available, reference data from Reyes *et al*. (2013) were also considered, while acknowledging that these correspond to a confined three-dimensional channel with a different confinement ratio. After these comparisons, simulations with different outlet conditions were performed to analyze and compare the power spectra associated with the various boundary conditions.

The computational implementation was developed in C++ with OpenMP for parallelization, while post-processing and analysis were performed using Python 3.8 scripts. The NumPy and SciPy libraries were employed for numerical data handling, and Matplotlib was used for graphical visualization. Flow field visualization was carried out in Paraview, providing a qualitative analysis complementary to the quantitative results.

3.2.1 Outlet boundary conditions

The accuracy and stability of LBM simulations strongly depend on the proper definition of boundary conditions, particularly at the outlet where artificial reflections can distort the flow field. To evaluate the influence of outlet treatment on the prediction of vortex shedding, four types of conditions were implemented: convective, null longitudinal velocity gradient, first-order extrapolation, and second-order extrapolation.

3.2.1.1 Convective

The convective boundary condition assumes that flow disturbances are transported out of the computational domain with a prescribed convection velocity (Lou *et al.*, 2013). It is mathematically expressed as

$$\frac{\partial \phi}{\partial t} + U \frac{\partial \phi}{\partial x} = 0, \tag{61}$$

where ϕ denotes a macroscopic variable and U represents the convection velocity.

In its discretized form, Lou *et al.* (2013) define the convective condition using a first-order finite-difference scheme as

$$f_i(\boldsymbol{x}, t) = \frac{f_i(\boldsymbol{x}, t - \Delta t) + U\, f_i(\boldsymbol{x} + \boldsymbol{c}_i \Delta t, t)}{1 + U}, \tag{62}$$

where $\boldsymbol{x}$ is the position of the outlet node.

The bulk velocity U can be computed according to

$$U = \begin{cases} U_{\max}(t) \equiv \max\{u(\boldsymbol{x} + \boldsymbol{c}_i, t)\}, \\ U_{\text{ave}}(t) \equiv \dfrac{1}{1+M} \sum_j u(\boldsymbol{x}, t), \\ U_{\text{local}}(t) \equiv u(\boldsymbol{x}, t). \end{cases} \tag{63}$$

These definitions yield three distinct measures of velocity, each associated with a different level of flow characterization. The first, $U_{\max}$, corresponds to the maximum velocity observed in the lattice column immediately upstream of the outlet. The second, U_{ave}, represents the average velocity over that same upstream column, providing a smoothed estimate of the flow. Finally, the local quantity U_{local} uses the macroscopic velocity at each lattice site in the upstream column and applies it directly to the corresponding outlet node.

Overall, this condition enables vortical structures to reach and cross the outlet boundary with minimal interference. It also reduces spurious reflections back into the computational domain (Breuer *et al.*, 2000).

3.2.1.2 Second-Order Extrapolation (SOE)

By borrowing ideas from the finite-difference methods for partial differential equations, some researchers were able to develop more general boundary schemes for such problems, and a good example is the second-order extrapolation (Chen *et al.*, 1996). This method refines the outlet treatment by considering information from the two nearest interior nodes, described as:

$$f_i(\boldsymbol{x}, t) = 2 f_i(\boldsymbol{x} + \boldsymbol{c}_i \Delta t, t) - f_i(\boldsymbol{x} + 2\boldsymbol{c}_i \Delta t, t). \tag{64}$$

This scheme better approximates the streamwise gradient of the distributions, providing a smoother continuation of the flow field at the outlet. However, is some cases leads to unstable solutions (Zhao-Li *et al*., 2002).

3.2.1.3 First-Order Extrapolation (FOE)

In order to mitigate the instabilities associated with higher-order outlet treatments, Dupuis (2002) adopts a first-order extrapolation scheme in which the unknown particle distribution functions at the boundary are simply copied from the adjacent interior node. This procedure represents a direct implementation of a zero-gradient condition at the outlet, consistent with the formulation described in Sec. 3.4.3 of Dupuis (2002). Formally, the extrapolation can be written as

$$f_i(\boldsymbol{x}, t) = f_i(\boldsymbol{x} + \boldsymbol{c}_i \Delta t, t), \tag{65}$$

where $\boldsymbol{x}$ denotes the outlet location and $\boldsymbol{x} + \boldsymbol{c}_i \Delta t$ corresponds to the last fluid node upstream along direction i. This condition assumes that the distribution functions vary negligibly in the streamwise direction, effectively enforcing a zero-gradient approximation.

3.2.1.4 Null Longitudinal Velocity Gradient (Null Gradient)

Following the idea of the FOE, the formulation presented in Section 3.4.4, Dupuis (2002) extends this approach by treating the outlet boundary through the imposition of a *null longitudinal velocity gradient* at the end of the channel. This condition is implemented by copying the particle distribution functions from the before last column into the last column, ensuring that the longitudinal variation of the flow remains minimal at the outlet. As pointed out by Dupuis (2002), a simple copy of the distributions would progressively increase the density at the boundary. To avoid this effect and to preserve global mass conservation, the copied fields are scaled proportionally to the density ratio between the outlet node and the adjacent interior node.

The resulting boundary condition is given by

$$f_i(\boldsymbol{x}, t) = \frac{\rho(\boldsymbol{x}, t)}{\rho(\boldsymbol{x} + \boldsymbol{c}_i \Delta t, t)}\, f_i(\boldsymbol{x} + \boldsymbol{c}_i \Delta t, t), \tag{66}$$

where $\boldsymbol{x}$ denotes the outlet location and $\boldsymbol{x} + \boldsymbol{c}_i \Delta t$ identifies the last interior fluid node aligned with direction i. In this expression, $\rho(\boldsymbol{x}, t)$ refers to the boundary density computed at the current time step, obtained using the same moment relations employed in standard Zou&He condition for the outlet on the right of the domain:

$$\rho(\boldsymbol{x}, t) = \frac{\displaystyle\sum_{i \in \mathcal{K}} f_i(\boldsymbol{x}, t) + 2 \sum_{j \in \mathcal{L}} f_j(\boldsymbol{x}, t)}{1 + u(\boldsymbol{x} + \boldsymbol{c}_i \Delta t, t)}, \tag{67}$$

where $\mathcal{K}$ and $\mathcal{L}$ denote, respectively, the sets of velocity directions whose discrete velocities satisfy $c_{ix} = 0$ (i.e., directions orthogonal to the boundary normal) and $c_{ix} > 0$ (i.e., incoming known populations at the right outlet). In a D2Q9 lattice, as seen in Figure 2, these sets reduce to $\mathcal{K} = \{0, 2, 4\}$ and $\mathcal{L} = \{1, 5, 8\}$, which recovers the standard Zou&He formulation. Finally, $\rho(\boldsymbol{x} + \boldsymbol{c}_i \Delta t, t)$ corresponds to the density evaluated at the adjacent interior node along the streaming direction.

As emphasized by Dupuis (2002), this condition prevents spurious density growth at the outlet and serves as an effective way to maintain a physically consistent outflow when employing velocity-based flow settlement strategies. Moreover, it significantly reduces the number of iterations required to obtain a stationary Poiseuille flow when compared to forcing strategies that impose pressure or body-force-driven profiles.

4 RESULTS AND DISCUSSIONS

4.1 BENCHMARK PLANE POISEUILLE

To ensure the reliability of the numerical implementation and to quantify the influence of boundary conditions on the solution, a plane Poiseuille flow benchmark was first simulated. This flow has an analytical solution, derived from the Navier–Stokes equations, expressed in terms of maximum velocity:

$$u(y) = U_{\text{max}} \left[1 - \left(\frac{y}{h} \right)^2 \right]. \tag{68}$$

Several combinations of inlet and outlet boundary conditions were evaluated to quantify the numerical error introduced by each approach. A fully developed velocity profile was initialized from Equation 68 in the inlet and compared with the numerical results, allowing an assessment of the deviations across different boundary treatments.

The computational meshes preserved the same proportions as the finest mesh proposed by Wang *et al*. (2015) (320 $\times$ 2000, in the H $\times$ L convention), but were rescaled to 60 $\times$ 375, 80 $\times$ 500, and 180 $\times$ 1125 to reduce computational cost. This approach allowed an analysis of mesh convergence while maintaining consistency with the reference study.

4.1.1 Velocity Error Analysis

The global velocity error was quantified using the L_2 norm

$$L_2 = \frac{\sqrt{\sum_{i=1}^{N_x} \sum_{j=1}^{N_y} \left(u_{ana}(i,j) - u_{num}(i,j) \right)^2}}{\sqrt{N_x N_y}}, \tag{69}$$

which measures the deviation of the numerical solution from the analytical profile across the entire computational domain.

Figure 13 presents the L_2 error for the inlet and outlet conditions as proposed by Zou and He (1997), providing an initial assessment of the numerical deviations. The convergence of the L_2 error with mesh refinement indicates that the numerical solution approaches the analytical profile, confirming the consistency and accuracy of the implementation. Furthermore, the slope of the curve shows a second-order decay rate, in agreement with the expected behavior reported in the literature for this class of boundary conditions.

Figure 14 compares the analytical Poiseuille profile with the numerical results obtained using three different meshes. The profiles show close agreement, with dis-

Figure 13 – Global L_2 error for Zou–He inlet/outlet boundary condition

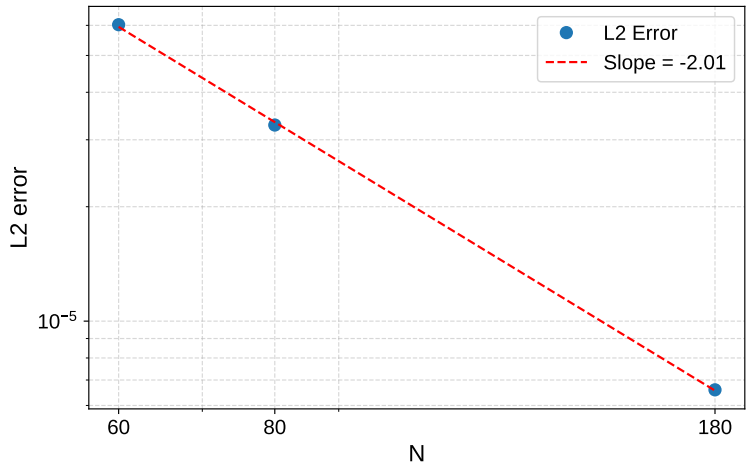

Source: Author (2025).

crepancies decreasing as the grid is refined, which further supports the convergence analysis.

Figure 14 – Comparison of Poiseuille profiles for different meshes and the analytical solution

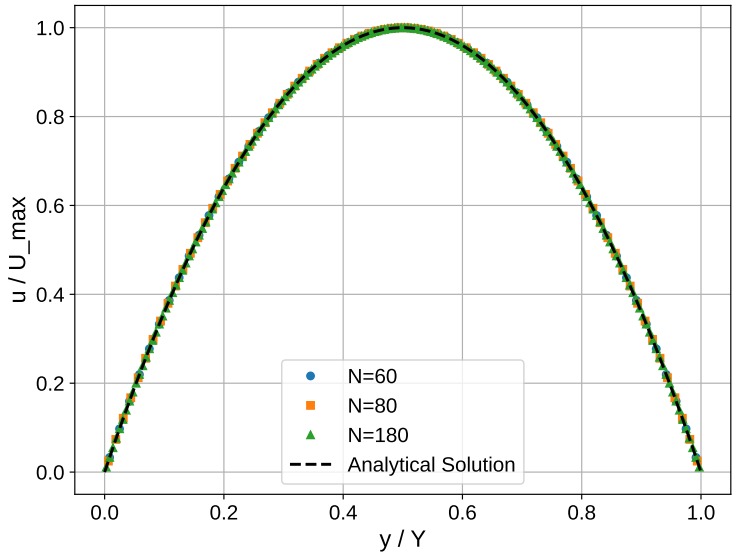

Source: Author (2025).

Table 2 summarizes the L_2 errors for all combinations of inlet and outlet boundary conditions. The results indicate that the convergence rate varies significantly across the different boundary treatments. In particular, the Breuer and FOE outlets showed a noticeably reduced rate of convergence, suggesting poorer agreement with the imposed inlet profile. In contrast, the Zou&He and Null Gradient outlets paired

with the Zou&He inlet delivered the highest convergence rates, reflecting better overall consistency within the numerical scheme.

Table 2 – L_2 error for all boundary condition combinations

Inlet \ Outlet	Zou&He	Breuer	Convective	FOE	SOE	Null Gradient
Zou&He	2.00	0.95	1.97	0.91	2.00	2.00
Breuer	0.96	0.96	1.05	0.91	1.26	0.96

Source: Author (2025).

In summary, the numerical implementation is able to reproduce the analytical Poiseuille profile with convergence rates up to second order, depending on the boundary condition combination. The configurations Zou&He + Zou&He, Zou&He + SOE and Zou&He + Null Gradient provide the most accurate and stable behavior, making them suitable choices for subsequent simulations.

4.1.2 Mass Conservation

In addition to velocity errors, the evaluation of mass accumulation in the domain is an important step in the simulation, because variations in total mass may lead to the appearance of non-physical phenomena. Since inlet and outlet boundary conditions can introduce such imbalances, an analysis was performed for the specific configurations used in this work.

To evaluate this effect, the same plane Poiseuille flow configuration used in the validation tests was adopted and the mass accumulation was quantified by computing the temporal variation of the total density in the domain, given by

$$\frac{\Delta M(t)}{M_o} = \frac{\sum_{x,y} \left[\rho(x,y,t) - \rho(x,y,0)\right]}{\sum_{x,y} \rho(x,y,0)},$$

where $\rho(x, y, t)$ denotes the local density at time t. All simulations were run for a total of $300s$ time steps for every combination of boundary conditions and mesh resolutions.

It is worth noting that the Zou & He and Breuer inlet conditions yielded identical mass accumulation rates. This behavior is possibly attributed to the fact that the flow is strictly imposed at the inlet, thereby making the global mass balance dependent on the performance of the outlet boundary condition. Given this equivalence, and to avoid redundancy, these two inlet cases are not explicitly distinguished in the data presented below.

The results presented in Table 3 show some degree of mass accumulation in all cases and reveal a notably larger increase when the FOE condition is applied. It is also observed that the boundary configurations exhibiting the highest accumulation

are those that use extrapolation of the distribution functions, which makes them more prone to introducing density imbalances.

Table 3 – Mass accumulation (%) for all boundary conditions and meshes

Outlet	Lattices across channel width		
	60	80	180
Zou&He	0.58%	0.29%	0.06%
Breuer	0.50%	0.29%	0.06%
Convective	4.13%	2.96%	1.20%
FOE	14.53%	11.09%	5.09%
SOE	3.73%	2.74%	1.17%
Null Gradient	0.72%	0.41%	0.08%

Given that the simulations are conducted in the incompressible regime, these small variations do not impact the velocity field. In incompressible LBM, the flow dynamics are governed primarily by the momentum distribution, making the observed mass growth negligible.

4.1.3 Numerical Stability at High Reynolds Numbers

While the velocity and mass errors were small for low Reynolds numbers, simulations at higher Reynolds numbers revealed numerical instabilities when the BGK collision operator was coupled with the Zou and He (1997) inlet condition. For $Re \approx 250$, density fluctuations originated near the inlet corners and were amplified along the entrance with time, eventually leading to numerical blow-up. Figure 15 illustrates the onset of these oscillations.

Figure 15 – Density fluctuations near the inlet for Zou&He condition at $Re = 300$

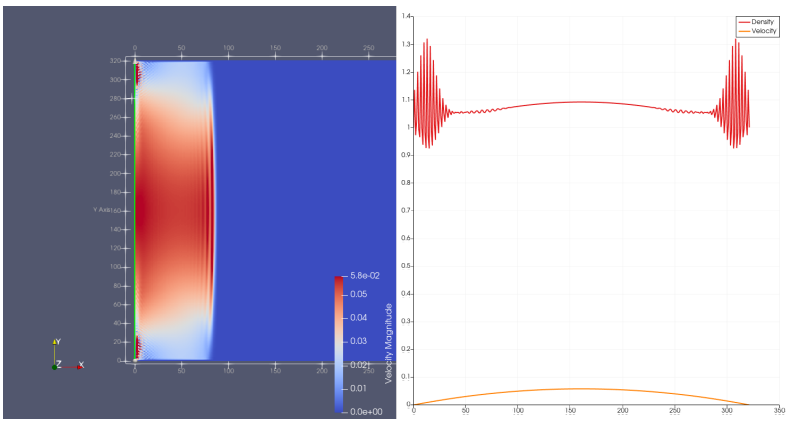

Source: Author (2025).

Attempts to initialize the field as fully developed or with a ramping of the inlet velocity were also unsuccessful, and the instabilities persisted. The most likely cause of this instability is the simpler relaxation structure of the BGK operator, which relies

on a single relaxation parameter and therefore lacks the additional degrees of control provided by the MRT model. This configuration produces an abrupt inlet condition that the BGK scheme, particularly when coupled with the Zou and He (1997) treatment of corner nodes, cannot properly handle, and even a mixed approach using Zou and He (1997) for the unknown distributions (f_1, f_5, and f_8) and bounce-back for the remaining ones (as shown in Figure 16) did not eliminate the instability.

Figure 16 – Density fluctuations near the inlet for Zou&He condition at $Re = 300$.

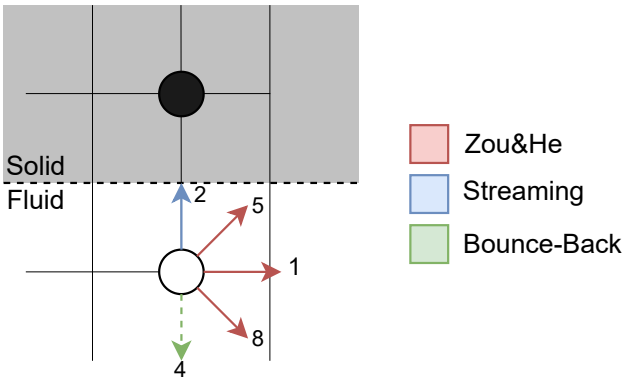

Source: Author (2025).

Consequently, the inlet condition proposed by Breuer *et al*. (2000) was adopted for the simulations that follow due to its stability at higher Reynolds number cases, even though it does not possess second-order accuracy. This limitation remains an open issue to be addressed in future work.

Overall, the benchmark demonstrates that the numerical implementation accurately reproduces the analytical Poiseuille solution, with convergence under mesh refinement and some mass accumulation. Additionally, the tests highlight the importance of selecting stable boundary conditions for high Reynolds number flows. These results provide a foundation for the subsequent comparison with the numerical simulations reported by Wang *et al*. (2015).

4.2 INTERNAL FLOW AROUND A SQUARE CYLINDER

4.2.1 Comparison with Wang *et al*. (2015)

In an effort to replicate the simulations conducted by Wang *et al*. (2015), this work employs a convective outlet boundary condition and an inlet boundary condition following the method proposed by Breuer *et al*. (2000) (as described in Section 3). The objective is to validate the implemented code by demonstrating that the physical behaviors reported in their work are successfully reproduced.

The analysis was carried out in two stages. First, a comparison between the LBM collision models and the Discrete Unified Gas Kinetic Scheme (DUGKS) was performed for low Reynolds numbers ($Re \leq 50$), corresponding to a flow regime without vortex shedding in the wake. Subsequently, simulations were conducted for higher Reynolds numbers ($60 \leq Re \leq 300$) to examine flow separation and unsteady behavior.

For the low-Reynolds-number cases, the analysis focused on the velocity profiles at different cross-sections and on the evaluation of the drag coefficient. Figure 17 summarizes the profiles obtained from these simulations.

Figure 17a shows the streamwise velocity component normalized by the maximum inlet profile velocity along the centerline of the channel from the inlet to the outlet. Figure 17b presents the streamwise velocity component normalized by the maximum profile velocity along the vertical axis crossing the center of the square obstacle from one domain wall to the other.

Figure 17c displays the transverse velocity component normalized by the maximum inlet profile velocity along the centerline of the channel from inlet to outlet. This plot exhibits a noticeable peak in the transverse velocity near the obstacle because the domain does not contain a lattice line exactly at the geometric center, which introduces a small numerical asymmetry.

Finally, Figure 17d shows the transverse velocity component along the vertical axis crossing the center of the square obstacle from one domain wall to the other.

Figure 17 – Velocity Profiles for $Re = 30$

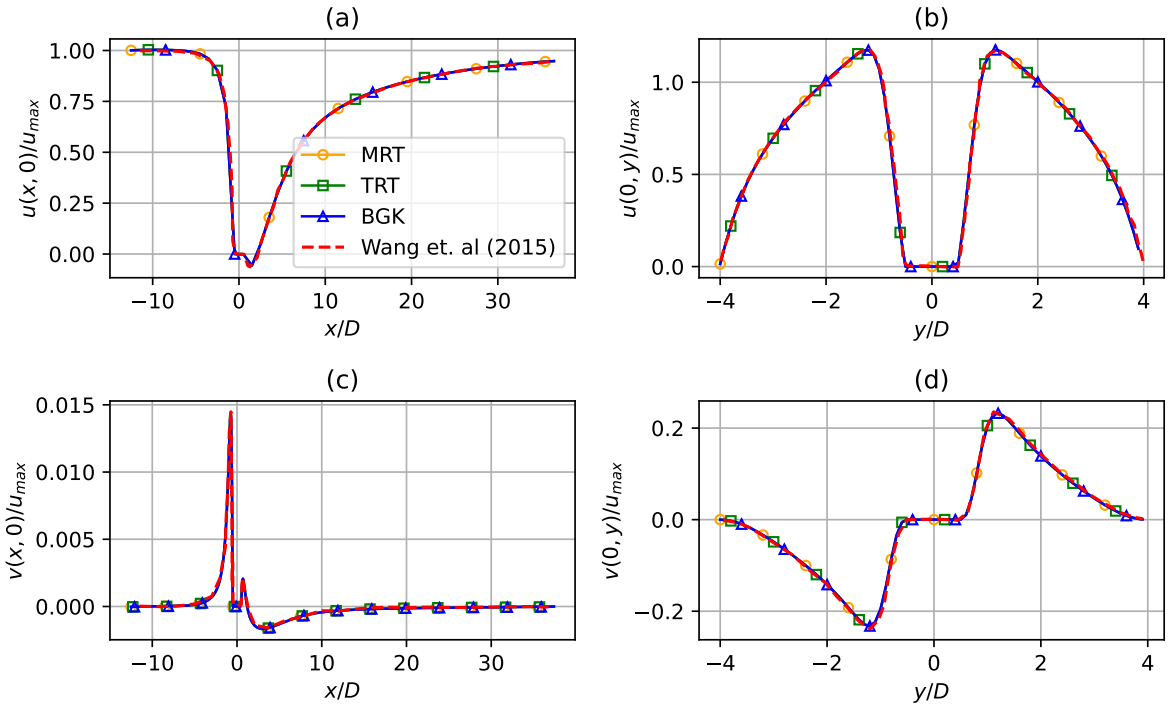

Source: Author (2025).

As observed, the BGK, MRT, and TRT collision operators all provide excellent agreement with the results reported by Wang *et al*. (2015) using the DUGKS method. This indicates that, for low Reynolds numbers without vortex shedding, the LBM is capable of accurately reproducing the flow velocity field.

Figure 18 shows the mean drag coefficient ($\bar{C}_d$) as a function of the Reynolds number. Once again, it can be seen that the LBM collision operators replicate the same flow behavior observed by Wang *et al*. (2015).

Figure 18 – Mean Drag Coefficient for $Re \leq 50$

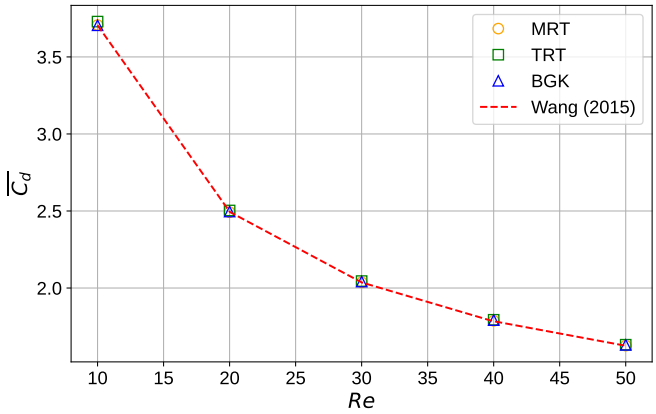

Source: Author (2025).

When entering the regime with vortex shedding, some differences in the mean drag coefficient ($\bar{C}_d$) are observed as the flow approaches the upper limit of the laminar regime for this problem. As shown in Figure 19, the LBM closely follows the data reported by Wang *et al*. (2015). It is interesting to note that the TRT model exhibits a slight deviation in this range and tends to approach the results of Breuer *et al*. (2000) at higher Reynolds numbers, which is consistent with the fact that the TRT formulation is designed to reduce wall-slip effects.

In addition to the mean drag coefficient, the variations of the drag (ΔC_d) and lift (ΔC_l) coefficients are analyzed. These variations are defined as the temporal fluctuations of each coefficient around its mean value and are computed as the standard deviation over a statistically steady interval of the simulation. In Figure 20, it can be seen that the lift coefficient predicted by the LBM remains consistent with the DUGKS up to $Re = 300$, where both methods deviate from the results of Breuer *et al*. (2000).

As shown in Figure 21, larger discrepancies are observed in ΔC_d among the LBM, DUGKS, and FVM results in $Re = 300$.

One may argue that the observed behavior could derive from three-dimensional effects. However, although phenomena such as spanwise instabilities are known to intensify wake unsteadiness for Reynolds numbers above 200, as demonstrated experi-

Figure 19 – Mean Drag Coefficient for $60 \leq Re \leq 300$

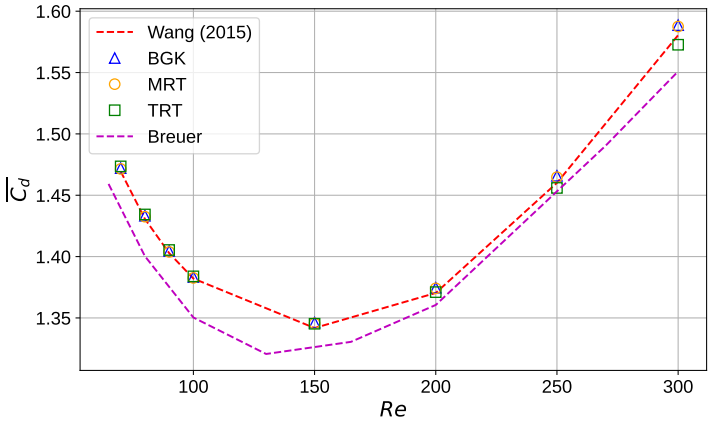

Source: Author (2025).

Figure 20 – Lift Coefficient Amplitude for $60 \leq Re \leq 300$

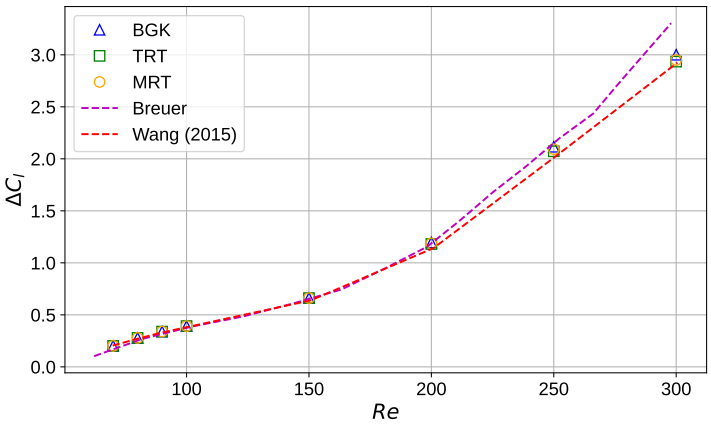

Source: Author (2025).

mentally and numerically by Sohankar *et al.* (1998), this mechanism cannot be invoked in the present study because all simulations were strictly two-dimensional.

When analyzing the Strouhal number over the studied Reynolds range, it is observed that the BGK and MRT collision operators show excellent agreement with the results of Wang *et al.* (2015) and Breuer *et al.* (2000). The TRT model also reproduces the same general trend of the Strouhal curve as the other collision operators.

Figure 22 shows that the results obtained over the studied Reynolds range present very good agreement for $Re < 200$. Above this range, however, the Strouhal number displays more pronounced deviations, both in comparison with the other collision operators and with the DUGKS and FVM data.

In the TRT model, the separation between the symmetric (ω^+) and antisymmetric (ω^-) relaxation rates allows for independent control of the viscous and dispersive effects of the flow. This adjustment provides greater flexibility to the model because

Figure 21 – Drag Coefficient Amplitude for $60 \leq Re \leq 300$

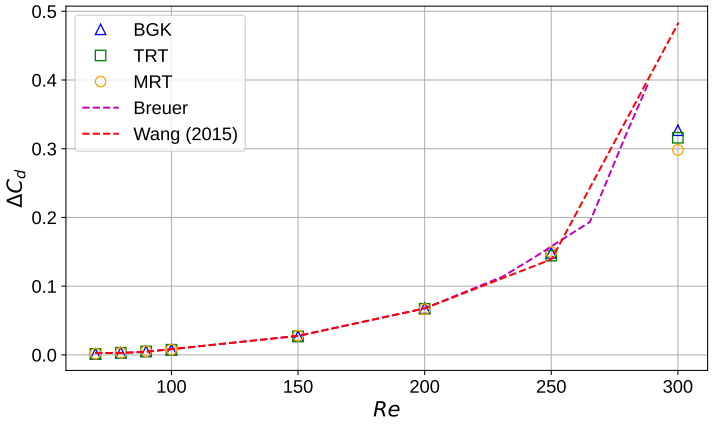

Source: Author (2025).

Figure 22 – Strouhal Number for $60 \leq Re \leq 300$

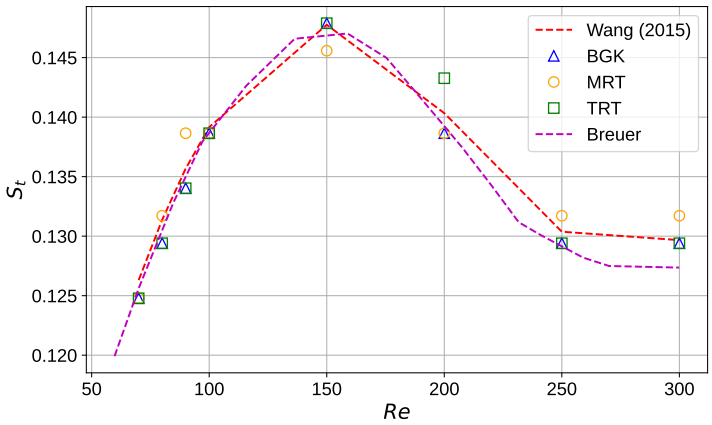

Source: Author (2025).

it can be tuned in different ways, including for increasing the stability and for reducing wall slip. However, Wang *et al*. (2015) did not perform simulations using this collision operator, which makes it difficult to establish an appropriate reference for parameter tuning.

In this work, ω^+ was calculated according to Equation 39, while the antisymmetric relaxation rate ω^- was chosen to be as close as possible to the odd-moment relaxation rates of the MRT model used by Wang *et al*. (2015). Consequently, the results indicate that the use of the TRT model must be approached with caution, since the second relaxation time—although not directly related to the viscosity—significantly affects the simulation outcome. It is important to note that when the two relaxation times are set equal, the TRT operator reduces to the BGK model and the results should therefore coincide.

Overall, despite the consistent trends observed among the BGK, MRT, and

TRT collision operators, the LBM results still present noticeable discrepancies when compared to the reference data from Wang *et al*. (2015) and Breuer *et al*. (2000), particularly for higher Reynolds numbers. These differences persist regardless of the chosen collision operator, indicating that other factors beyond the relaxation scheme may significantly influence the numerical accuracy of the method.

Therefore, since the LBM theoretically recovers the Navier–Stokes equations in the low-Mach-number regime, where the flow behaves as nearly incompressible, it is reasonable to assume that the observed discrepancies arise from the treatment of the inlet and outlet boundary conditions. For this reason, the following section focuses on a detailed investigation of these boundary-condition implementations in the LBM formulation, aiming to assess their direct impact on the predictive capability and stability of the simulations.

4.2.2 Boundaries

After validating the code through the benchmark in Section 4.1 and comparing it with the results of Wang *et al*. (2015), this subsection analyzes how different outlet boundary conditions—Convective, Null Gradient, and First-Order Extrapolation (FOE)—affect vortex shedding and the spectral response of the lift coefficient. The Second-Order Extrapolation (SOE) condition was excluded due to numerical instabilities at $Re > 250$.

The evaluation is based on the PSD of the lift coefficient C_l, obtained from the Fourier transform of its time history. The procedure begins by reading the temporal signal $C_l(t)$ and converting lattice quantities into physical units using the characteristic simulation scales, after which the mean value is removed so that only the fluctuating component contributes to the spectral analysis.

The signal is decomposed as

$$C_l'(t) = C_l(t) - \overline{C_l}, \tag{70}$$

where $\overline{C_L}$ is the temporal average, ensuring that the spectrum reflects only oscillatory content. The fluctuation field $C_l'(t)$ is then processed using the Welch method, which computes the Power Spectral Density (PSD) as

$$\Phi_{C_l}(f) = \frac{1}{N_w} \sum_{k=1}^{N_w} \frac{1}{f_s\, L} \left| \mathcal{F}\{w(t)\, C_l'(t)\}_k \right|^2, \tag{71}$$

with $w(t)$ denoting the Hann window, f_s the sampling frequency and N_w the number of overlapping segments, which reduces variance and yields a smooth and well-resolved estimate of the dominant frequencies. This enables the identification of the principal shedding frequency, as well as secondary oscillation modes that may emerge for certain boundary-condition choices or Reynolds numbers.

To isolate the influence of the outlet boundary conditions, simulations were performed for each configuration using all available collision operators. This procedure verified whether the choice of collision model affects the vortex-shedding behavior or alters the frequency spectrum.

Figure 23 groups the three vorticity fields, where panel (a) shows the convective boundary condition, panel (b) the Null Gradient condition, and panel (c) the FOE treatment, allowing a direct comparison of their wake behaviors. The convective case in panel (a) exhibits a well-defined Kármán vortex street with alternating vortices that decay smoothly downstream, whereas the Null Gradient case in panel (b) shows slight irregularities near the outlet that suggest partial reflections, and the FOE case in panel (c) presents similarly mild deformations with distortions marginally lower than those observed for the Null Gradient condition.

Figure 23 – Cropped mid-plane vorticity field.

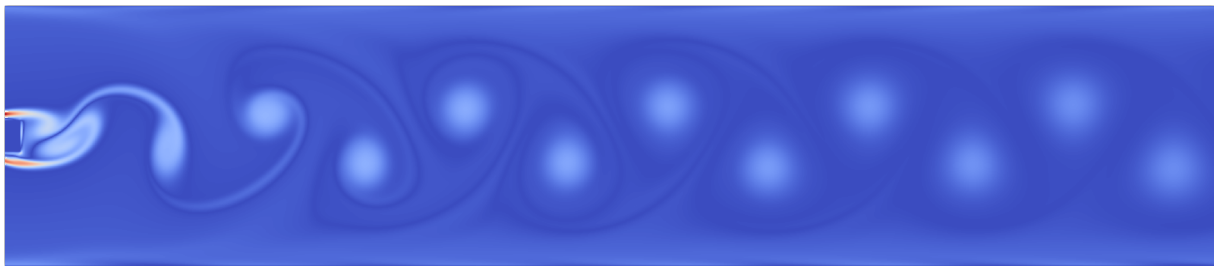

(a) Convective

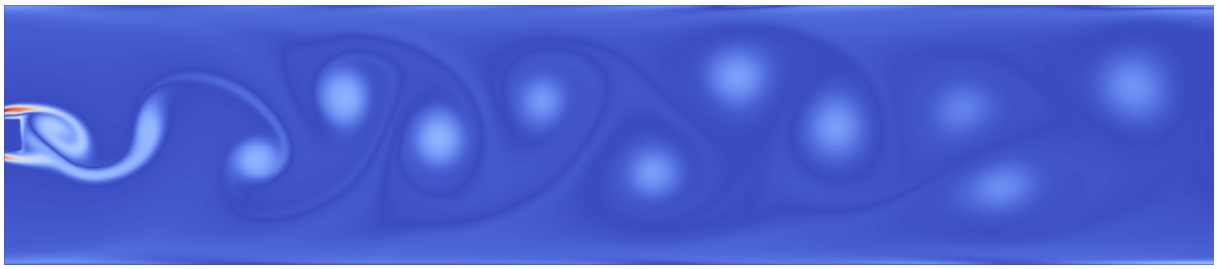

(b) Null Gradient

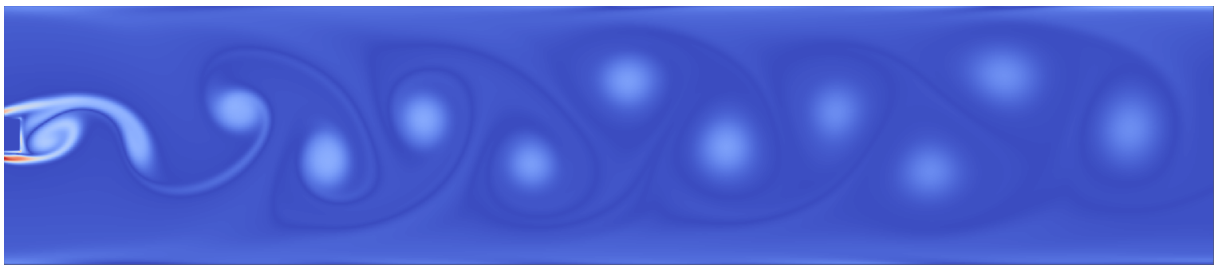

(c) FOE

Source: Author (2025).

This combined visualization provides a qualitative assessment of the wake dynamics prior to the quantitative analysis conducted through the PSD. This context high-

lights how the flow behavior observed in the vorticity fields guides the interpretation of subsequent spectral results.

To complement this analysis, Wang *et al*. (2015) presents in his work Figure 24, which compares side by side the time history of drag and lift coefficients from a simulation using the DUGKS (a) and another using the BGK lattice Boltzmann model (LBGK) (b). In that figure, the LBGK results show no indication of a secondary frequency in the oscillation, whereas the DUGKS results clearly exhibit additional oscillatory modes.

Figure 24 – Time history of the drag coefficient C_d and lift coefficient C_l at $Re = 300$.

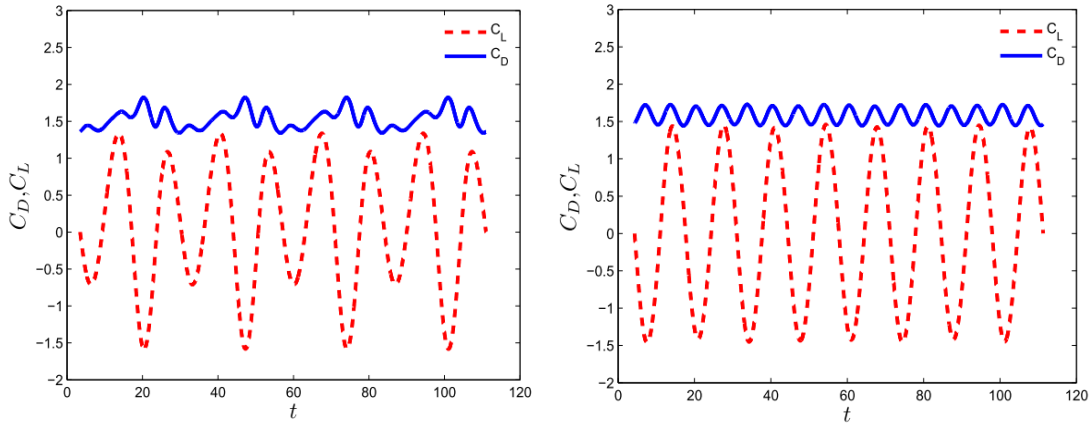

(a) DUGKS (b) LBGK

Source: Wang *et al*. (2015).

Building upon these qualitative observations, a quantitative investigation of the oscillatory modes is now performed through the PSD analysis. Figure 25 presents the PSD for the convective boundary condition, where this treatment allows disturbances to exit the computational domain smoothly, minimizing reflections and ensuring stable wake development downstream of the obstacle.

The spectra obtained for all collision operators—BGK, MRT, and TRT—display nearly identical distributions of fluctuation energy, with a single dominant frequency associated with periodic vortex shedding. This behavior is consistent with the vorticity field in Figure 23a, which shows a well-organized Kármán vortex street and gradual dissipation of structures near the outlet, evidencing the efficiency of this condition.

Figure 26 presents the PSD for the Null Gradient boundary condition. The results obtained for different collision operators show overall good agreement across the frequency range, with deviations at high frequencies that are likely associated with the reflections observed in the vorticity field.

This formulation behaves as a temporal extrapolation of the outgoing distributions, assuming that the downstream evolution follows that of the upstream node. Although it preserves continuity and does not completely eliminate reflections, it corrects

Figure 25 – Power Spectral Density (PSD) for Convective at $Re = 300$

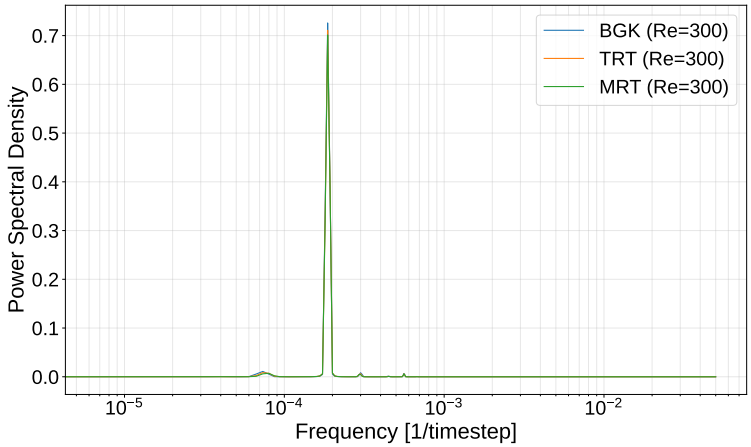

Source: Author (2025).

Figure 26 – Power Spectral Density (PSD) for Null Gradient at $Re = 300$

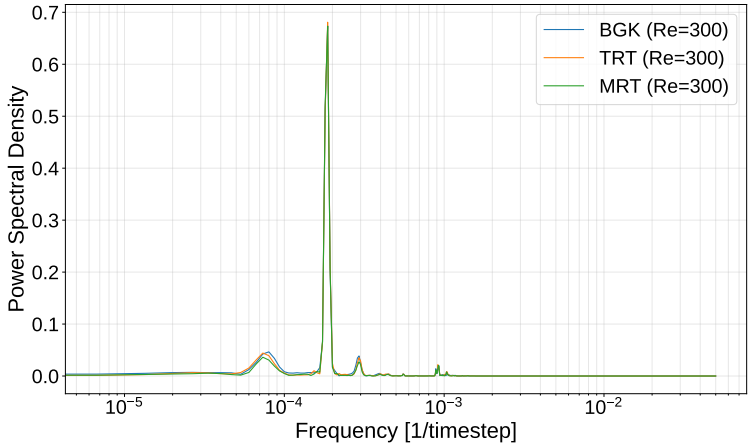

Source: Author (2025).

the mass accumulation problem observed in the FOE due to the correction coefficient in the formulation.

Figure 27 presents the PSD for the FOE boundary condition. The spectra show strong agreement among all collision operators, with consistent energy distribution across the frequency range. A distinct increase in energy appears at frequencies below the primary peak, indicating a possible secondary oscillation mode. In contrast, the smaller peaks at higher frequencies are likely caused by reflections at the outlet boundary.

Finally, Figure 28 compares the PSD of the lift coefficient C_l for the Convective, Null Gradient, and FOE outlet conditions at $Re = 300$ using the MRT. The Convective condition exhibits the highest amplitude at the primary frequency, showing a well-defined dominant shedding mode with almost no secondary components, aside

Figure 27 – Power Spectral Density (PSD) for FOE at $Re = 300$

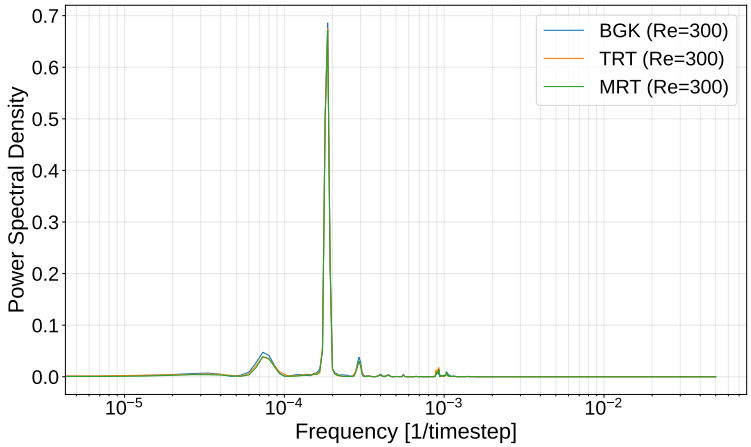

Source: Author (2025).

from a slight rise near 7×10^{-5} that marks the onset of a weak secondary frequency also present in the other conditions.

Figure 28 – PSD of All Boundaries at $Re = 300$ (MRT)

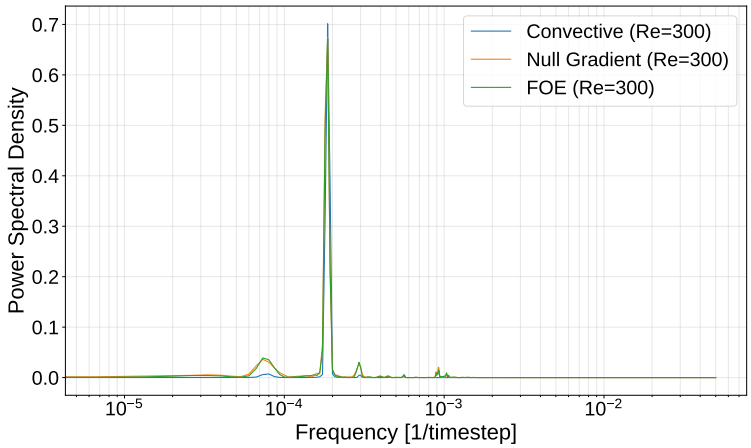

Source: Author (2025).

The Null Gradient and FOE boundaries follow this same primary shedding frequency, but they differ from the Convective case by presenting higher amplitudes at frequencies below the primary. Both conditions also share nearly identical spectral shapes, including a small peak at higher frequencies near 9×10^{-4} that does not appear in the Convective spectrum and is likely associated with reflections generated at the outlet boundary.

In summary, the results demonstrate that the choice of outlet boundary condition significantly affects the spectral characteristics of the flow. The Convective condition provides the most stable behavior with minimal interference, while the Null Gradient exhibits spectral characteristics comparable to the FOE treatment and simultane-

ously prevents the mass-accumulation effects associated with FOE. The FOE condition maintains a balanced performance with partial mitigation of reflections and coherent flow behavior, and both FOE and Null Gradient display higher-frequency components with similarly amplitudes. These findings highlight the importance of proper boundary treatment for accurately capturing the unsteady dynamics of confined vortex shedding.

4.2.3 Comparison with Experiments from Reyes *et al*. (2013)

A detailed experimental investigation of the confined three-dimensional laminar flow past a square prism was conducted by Reyes *et al*. (2013) for Reynolds numbers ranging from 100 to 256. The channel had a square cross-section of 25×25 mm, while the obstacle had a side length of 10 mm, resulting in a high blockage ratio of $1 : 2.5$ and an aspect ratio of $1 : 1$. The experiments were performed in a closed-loop water channel using Particle Image Velocimetry (PIV) to obtain detailed velocity fields in multiple planes along the flow domain. Figure 29 presents a schematic view of the experimental setup, illustrating the test section geometry and measurement configuration described by the authors.

Figure 29 – Schematic view of the experimental setup.

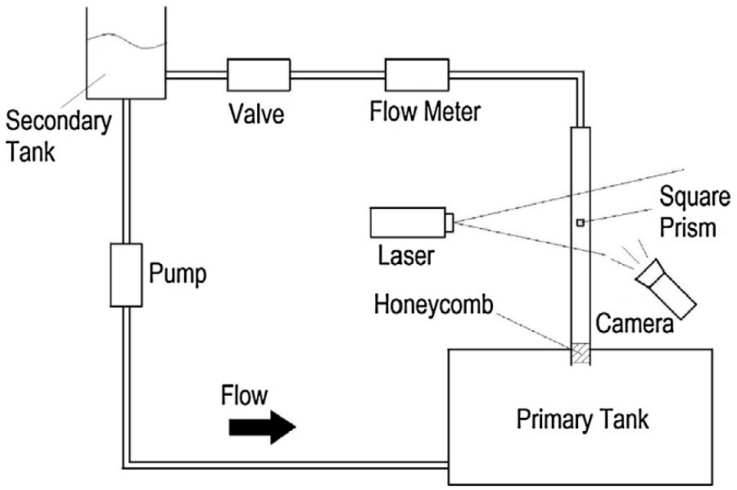

Source: Reyes *et al*. (2013).

The results demonstrated that lateral confinement exerts a strong influence on flow topology, delaying the onset of vortex shedding to Reynolds numbers near 170, in contrast to unconfined cases where the transition occurs between 50 and 60. Three distinct regimes were identified: a steady recirculation bubble for $Re < 120$, a pulsating bubble for $120 \leq Re \leq 170$, and a periodic vortex-shedding regime for $Re > 170$. Furthermore, the shedding frequency remained nearly constant throughout the unsteady regime ($Re > 170$), with the parameter $St \times Re$ varying between 67.4 and 73.2, where Reyes *et al*. (2013) assign this behavior to the fact that three-dimensional

confinement modifies the oscillatory behavior typically observed in two-dimensional configurations.

Given the absence of experimental data in transitional regime, the work of Reyes *et al*. (2013) provides a valuable reference for validation. Therefore, the present section includes a direct comparison between the numerical simulations and the experimental observations reported by Reyes *et al*. (2013), aiming to evaluate the accuracy of the model in reproducing the main flow features and frequency characteristics.

The simulation was conducted in a two-dimensional domain using the same reference scales as Wang *et al*. (2015), but with an aspect ratio of $1/2.5$ consistent with the experimental configuration. To enhance numerical stability in this setting, the collision step employed the MRT operator, whose relaxation coefficients were set to $S_e = 1.64$, $S_\epsilon = 1.54$, $S_{qx} = 1.2$, $S_{qy} = 1.2$, and $S_{pxx} = S_{pxy} = 1/(3\nu + 0.5)$. The outlet boundary conditions evaluated in the previous section—Convective, Null Gradient, and FOE—were likewise incorporated into the present simulation to assess their behavior under this configuration.

Before presenting the comparison, a Grid Convergence Index (GCI) analysis was performed to verify the spatial independence of the numerical results. This technique assumes that the discretization error depends on the grid spacing through a power law, whose exponent corresponds to the observed order of convergence, providing a quantitative estimate of the asymptotic solution and the uncertainty associated with grid refinement (Roache, 2009). The observed order of convergence p is calculated from three successively refined meshes as

$$p = \frac{\ln\left(\dfrac{\phi_3 - \phi_2}{\phi_2 - \phi_1}\right)}{\ln(r)} \,, \tag{72}$$

where ϕ_1, ϕ_2, and ϕ_3 are the numerical solutions obtained on the fine, medium, and coarse grids, respectively, and r is the grid refinement ratio ($r = h_2/h_1 = h_3/h_2$). Once p is known, the extrapolated value ϕ_{ext} can be estimated by

$$\phi_{\text{ext}} = \phi_1 + \frac{\phi_1 - \phi_2}{r^p - 1} \,, \tag{73}$$

and the Grid Convergence Index for the fine grid is obtained as

$$\text{GCI}_{\text{fine}} = F_s \frac{|\phi_1 - \phi_2|}{\phi_1(r^p - 1)} \times 100\% \,, \tag{74}$$

which represents an estimate of the relative discretization error multiplied by the safety factor F_s, commonly set to 1.25 for three-grid comparisons. This analysis ensures that the numerical solution lies within the asymptotic range of convergence, providing confidence that mesh-related errors are negligible in the subsequent comparison.

For the GCI analysis, three grids were employed at $Re = 170$: one with a square obstacle of 40 lattice units per side, another with 60 lattice units, and the finest grid with 90 lattice units. The results obtained from the three-mesh GCI procedure are summarized in Table 4, and the observed order of convergence shows excellent agreement, likely because all grids used were already sufficiently refined for the flow configuration considered.

Table 4 – GCI Analysis for Experimental Case.

Case	**Re**	**Mesh**	r	p	$\phi_{\text{ext}}(C_D)$	GCI [%]	**Convergence order**
1	170	M1 - M2 M2 - M3	1.5	5.21450043	2.44849563	0.005765 0.047739	1.000336

This assessment confirmed that the solution is within the asymptotic range of convergence, indicating that discretization errors are sufficiently small for the subsequent comparison with experimental data.

Once grid independence was verified, the Power Spectral Density (PSD) analysis was performed. In the approach of Reyes *et al*. (2013), the PSD is computed from a streamwise velocity signal extracted from a point (P1) located downstream of the cube, as illustrated in Figure 30. The velocity at this point was monitored over time and used to compute the PSD, allowing the identification of the dominant frequency components associated with vortex shedding. A complete conversion from physical to lattice units was carried out to ensure that all geometric and flow parameters were properly scaled for direct comparison between the experimental and numerical results.

Figure 30 – Schematic view of the experimental setup.

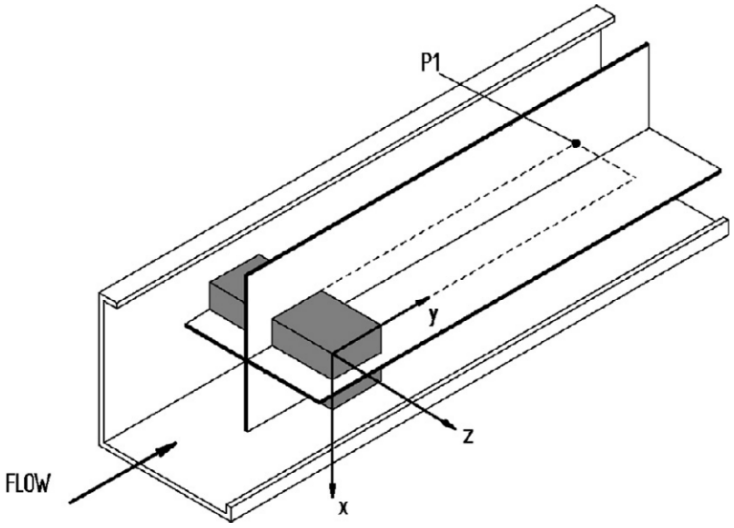

Source: Reyes *et al*. (2013).

The experimental PSD curves presented by Reyes *et al*. (2013) were digitized for direct comparison with the numerical simulations performed in this work. The pri-

mary shedding frequency obtained from the simulations was extracted directly from the numerical PSD curve.

Table 5 summarizes the Strouhal numbers obtained from both sources, including the product $St \times Re$ and the percentage deviation between simulation and experiment. These results correspond to the configuration employing the convective outflow boundary condition.

This comparison allows a direct quantitative evaluation of the LBM performance in reproducing the experimental vortex shedding dynamics. It also provides a consistent basis for analyzing the influence of boundary conditions and flow parameters on the oscillatory behavior, as discussed in the subsequent analysis.

Table 5 – Relationship between St and Re.

Re	$f_p\ [Hz]$	$(f_p)_{Exp.}\ [Hz]$	St	$St_{Exp.}$	$St\ x\ Re$	$(St\ x\ Re)_{Exp.}$	Error [%]
160	0.684	0.681	0.427	-	68.37	-	0.368
205	0.729	0.736	0.356	0.357	73.0	73.2	0.829
256	0.706	0.699	0.276	0.273	70.603	69.9	0.934

The results in Table 5 show that the relative error in the primary frequency is very low, confirming that the LBM accurately reproduces the dominant shedding frequency. However, since the present simulation is two-dimensional, an inherent limitation must be acknowledged, as three-dimensional experimental effects can introduce additional dynamics that are not represented in the numerical model.

As shown in Figure 31, other oscillation modes present in the experimental PSD are not well captured by the simulation, and although some secondary peaks appear at similar frequencies, their amplitudes and exact positions differ from those observed experimentally. This discrepancy indicates that the numerical model can only partially reproduce the multi-frequency behavior of the flow, a limitation that is consistent with the reduced dimensionality of the simulation.

It can also be observed that, for this confinement ratio, the outlet boundary condition does not significantly affect the oscillation modes of the vortices. The flow remains dominated by the primary shedding mechanism, and variations between boundary treatments result mainly in minor amplitude differences rather than frequency shifts. This behavior suggests that, under more confined conditions, the feedback effects from the outlet are less pronounced, since the channel walls dominate the flow dynamics.

Overall, these results confirm the ability of the LBM with MRT collision operator to accurately reproduce the dominant shedding frequency observed experimentally for confined flow. However, the discrepancies in secondary modes reveal the sensitivity of more complex flow structures to boundary effects and three-dimensional influences not fully captured by the two-dimensional model. Further investigation is required to de-

Figure 31 – PSD comparison between boundary-condition simulations and experimental data.

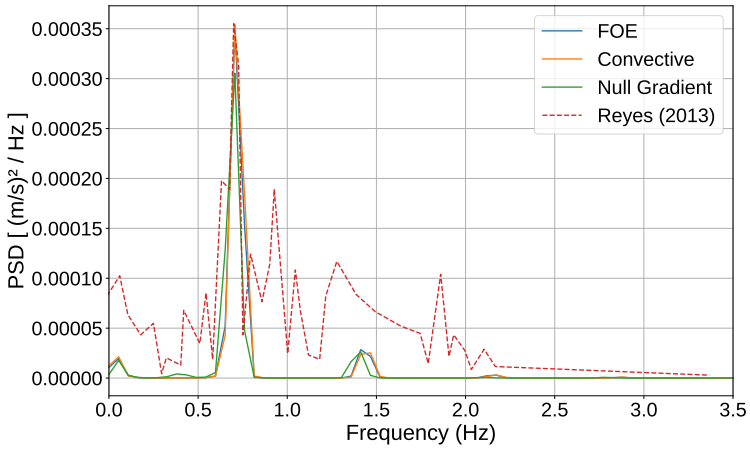

Source: Author (2025).

Figure 32 – Velocity flow field - $Re = 256$.

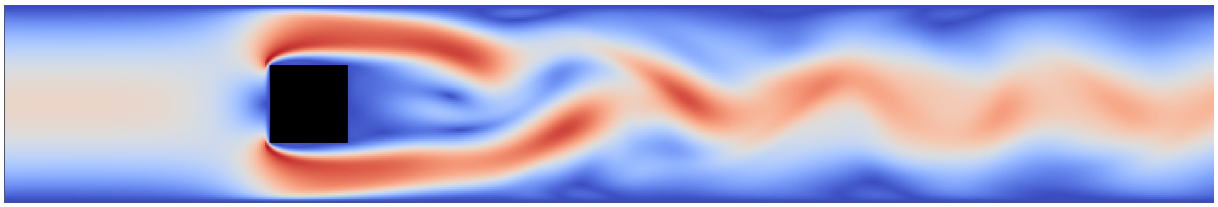

Source: Author (2025).

termine whether these differences arise from from numerical limitations, confinement effects, or experimental uncertainties.

5 CONCLUSION

The present work evaluated the influence of outlet boundary conditions on the ability of the Lattice Boltzmann Method (LBM) to reproduce vortex shedding phenomena in confined laminar flows past a square obstacle. It combined theoretical formulation, numerical implementation, and validation through benchmark and comparative analyses with numerical and experimental references.

In this context, the implementation of a C++ code, validated through a plane Poiseuille flow benchmark where the convergence order of each boundary condition was analyzed, enabled the evaluation of different boundary conditions, including Convective, Null Gradient, First-Order, and Second-Order Extrapolation, together with BGK, MRT, and TRT collision operators.

The results showed that the present implementation, which employs the inlet condition proposed by Breuer *et al*. (2000), achieved at most first-order spatial accuracy for all boundary conditions tested, including the convective one used by Wang *et al*. (2015), and this choice was necessary because the Zou and He (1997) condition caused instabilities when combined with the BGK operator. In practical applications, however, the analysis indicates that the combination of the Zou and He (1997) inlet condition with a convective outlet yields the highest convergence order and offers the most accurate configuration among those evaluated.

Regarding the specific objectives established for this work, the formation and evolution of vortical structures were quantitatively characterized from the lift coefficient and vorticity fields, allowing the identification of periodic shedding and flow regimes. The comparative analysis among BGK, MRT, and TRT collision operators demonstrated consistent reproduction of the main flow characteristics, and since no significant accuracy differences were observed, choosing the MRT operator appears more advantageous due to its improved stability. The Fourier analysis enabled the identification of dominant frequencies and the evaluation of secondary modes, confirming that outlet boundary conditions have a significant impact on the spectral response. The implementation and assessment of different boundary schemes revealed that the Convective condition provides the most stable behavior with minimal reflections, while the Null Gradient and First-Order Extrapolation introduce subharmonic peaks.

Comparisons with the results of Wang *et al*. (2015) demonstrated that the LBM accurately reproduces velocity profiles, drag coefficients, and primary vortex-shedding frequencies for Reynolds numbers up to 300. Nonetheless, increasing discrepancies in lift and drag amplitudes were observed at higher Reynolds numbers.

However, as observed in the work of Wang *et al*. (2015), the emergence of secondary frequencies in the vortex wake was reported for the DUGKS method and

other finite-volume approaches, which are not identified in the same manner in LBM. These deviations may be related to the influence of the outlet boundary conditions employed, but in the current stage of this study a definitive cause cannot be established, making a more recent experimental investigation valuable for further clarification.

The spectral analysis highlighted that the choice of outlet boundary condition strongly affects the energy distribution of the Power Spectral Density (PSD). The Convective condition yielded the most stable and reflection-free behavior, while the Null Gradient and First-Order Extrapolation conditions introduced low-frequency subharmonic peaks associated with partial reflections at the outlet, and the Null Gradient condition also corrects the mass accumulation problem observed in the FOE. In contrast, the Second-Order Extrapolation condition, although more accurate in theory, exhibited numerical instabilities at higher Reynolds numbers, leading to divergence and thus limiting its applicability to confined laminar flow simulations.

When compared with the experimental data of Reyes *et al*. (2013), the simulations using the MRT operator reproduced the dominant shedding frequency with relative errors below one percent. However, secondary modes were not fully captured, indicating that confinement and three-dimensional effects dominate the flow behavior and limit the representativeness of two-dimensional simulations.

These findings confirm that the LBM, when properly configured, is capable of accurately predicting the primary vortex shedding dynamics in confined laminar flows. Nevertheless, the method remains sensitive to boundary treatments and dimensional simplifications, which constrain its ability to capture higher-order oscillatory structures observed experimentally.

In addition, the independent development of the numerical code reinforced the understanding of the objectives proposed in this research, demonstrating that the LBM is a computational method of relatively simple implementation. This process not only confirmed the feasibility of applying the method to confined flow problems but also deepened the understanding of its physical foundations.

5.1 FUTURE WORKS

The present work compared different boundary conditions with both numerical and experimental results available in the literature. To refine the current work and advance research on boundary conditions and their influence on the flow field, aiming to further consolidate the LBM as a reliable tool for aerodynamic flow simulations, the following research directions are proposed:

- Investigation and implementation of non-reflective boundary conditions available in the literature.

- Implementation of the boundary condition proposed by Bouzidi *et al*. (2001) for curved surfaces to extend the study for more complex cylinder geometries.
- Analysis of three-dimensional effects on confined flow through numerical simulations.
- Execution of experiments within the Reynolds number range evaluated in this work using a recirculating water channel to obtain up-to-date experimental data.

BIBLIOGRAPHY

BEARMAN, P.; OBASAJU, E. D. An experimental study of pressure fluctuations on fixed and oscillating square-section cylinders. **Journal of Fluid Mechanics**, 1982.

BEARMAN, P. W.; TRUEMAN, D. M. An investigation of the flow around rectangular cylinders. **Aeronautical Quarterly**, v. 23, p. 229–237, ago. 1972.

BHATNAGAR, P. L.; GROSS, E. P.; KROOK, M. A model for collision processes in gases. i. small amplitude processes in charged and neutral one-component systems. **Phys. Rev.**, American Physical Society, v. 94, p. 511–525, May 1954. Disponível em: https://link.aps.org/doi/10.1103/PhysRev.94.511.

BOUZIDI, M.; FIRDAOUSS, M.; LALLEMAND, P. Momentum transfer of a Boltzmann-lattice fluid with boundaries. **Physics of Fluids**, American Institute of Physics Inc., v. 13, n. 11, p. 3452–3459, 2001. ISSN 10706631.

BREUER, M. *et al.* Accurate computations of the laminar flow past a square cylinder based on two different methods : lattice-boltzmann and finite-volume. **International Journal of Heat and Fluid Flow**, 2000.

CHEN, S.; DOOLEN, G. D. Lattice boltzmann method for fluid flows. **Annual Review of Fluid Mechanics**, v. 30, n. 1, p. 329–364, 1998.

CHEN, S.; MARTINEZ, D.; MEI, R. On boundary conditions in lattice boltzmann methods. **Physics of fluids**, American Institute of Physics, v. 8, n. 9, p. 2527–2536, 1996.

CHEN, Z.; SHU, C.; TAN, D. S. A truly second-order and unconditionally stable thermal lattice boltzmann method. **Applied Sciences**, MDPI, v. 7, n. 3, p. 282, 2017. Disponível em: https://www.mdpi.com/2076-3417/7/3/282.

DAVIS, R. W.; MOORE, E.; PURTELL, L. A numerical-experimental study of confined flow around rectangular cylinders. 1984.

D'HUMIÈRES, D. Generalized Lattice-Boltzmann Equations, Rarefied Gas Dynamics: Theory and Simulations. **Progress in Astronautics and Aeronautics**, v. 159, p. 450–458, 1992.

D'HUMIÈRES, D. time lattice boltzmann models in three- relaxation- multiple. **Phil. Trans. R. Soc. Lond. A**, v. 360, p. 437–451, 2002.

DUPUIS, A. **From a lattice Boltzmann model to a parallel and reusable implementation of a virtual river**. 2002. Thesis (Doctorate) — UNIVERSITÈ DE GENÈVE, 2002. Disponível em: http://citeseerx.ist.psu.edu/viewdoc/download?doi=10.1.1.386.7839&rep=rep1&type=pdf.

GELLER, S.; KRAFCZYK, M.; TÖLKE, J.; TUREK, S.; HRON, J. Benchmark computations based on lattice-Boltzmann, finite element and finite volume methods for laminar flows. **Computers Fluids**, v. 35, n. 8, p. 888–897, 2006. ISSN 0045-7930. Disponível em: https://www.sciencedirect.com/science/article/pii/S0045793005001519.

GINZBURG, I.; D'HUMIÈRES, D.; KUZMIN, A. Optimal stability of advection-diffusion lattice boltzmann models with two relaxation times for positive/negative equilibrium. **Journal of Statistical Physics**, Springer, v. 139, n. 6, p. 1090–1143, 2010.

GINZBURG, I.; VERHAEGHE, F.; D'HUMIERES, D. Two-relaxation-time lattice boltzmann scheme: About parametrization, velocity, pressure and mixed boundary conditions. **Communications in computational physics**, v. 3, n. 2, p. 427–478, 2008.

GUO, Z.; SHU, C. **Lattice Boltzmann method and its application in engineering**. [S.l.]: World Scientific, 2013. v. 3.

HE, X.-J.; LUO, L.-S. Theory of the lattice boltzmann method: From the boltzmann equation to the lattice boltzmann equation. **Physical Review E**, American Physical Society, v. 56, n. 6, p. 6811–6817, 1997.

HOMANN, F. Einfluß großer zähigkeit bei strömung um zylinder. **Forschung Im Ingenieurwesen-engineering Research**, 1936.

HOU, S.; STERLING, J.; CHEN, S.; DOOLEN, G. A lattice boltzmann subgrid model for high reynolds. **Pattern formation and lattice gas automata**, American Mathematical Soc., v. 6, n. 6, p. 151, 1996.

KRÜGER, T. *et al*. **The Lattice Boltzmann Method principles and practice**. Switzerland: Springer, 2017. 0-694 p.

KUNDU, P. K.; COHEN, I. M.; DOWLING, D. R.; CAPECELATRO, J. **Fluid mechanics**. [S.l.]: Elsevier, 2024.

KáRMáN, T. v. Ueber den mechanismus des widerstandes, den ein bewegter körper in einer flüssigkeit erfährt. **Nachrichten von der Gesellschaft der Wissenschaften zu Göttingen, Mathematisch-Physikalische Klasse**, v. 1911, p. 509–517, 1911. Disponível em: http://eudml.org/doc/58812.

LADD, A. J. Numerical simulations of particulate suspensions via a discretized boltzmann equation. part 1. theoretical foundation. **Journal of fluid mechanics**, Cambridge University Press, v. 271, p. 285–309, 1994.

LOU, Q.; GUO, Z.; SHI, B. Evaluation of outflow boundary conditions for two-phase lattice boltzmann equation. **Physical Review E—Statistical, Nonlinear, and Soft Matter Physics**, APS, v. 87, n. 6, p. 063301, 2013.

MOHAMAD, A. A. **Lattice Boltzmann Method: Fundamentals and Engineering Applications with Computer Codes**. [S.l.: s.n.], 2013. v. 51. 278–279 p. ISSN 0001-1452. ISBN 9780857294548.

MUKHOPADHYAY, A.; BISWAS, G.; SUNDARARAJAN, T. Numerical investigation of confined wakes behind a square cylinder in a channel. 1992.

NAKAGUCHI, H.; HASHIMOTO, K.; MUTO, S. An experimental study on aerodynamic drag of rectangular cylinders. 1968.

NOELTING, S.; FARES, E. The Lattice-Boltzmann Method: An Alternative to les for Complex Aerodynamic and Aeroacoustic Simulations in the Aerospace Industry. **SAE Technical Papers**, v. 2015-September, n. September, 2015. ISSN 01487191.

OKAJIMA, A. Strouhal numbers of rectangular cylinders. **Journal of Fluid Mechanics**, 1982.

QIAN, Y. H.; D'HUMIèRES, D.; LALLEMAND, P. Lattice bgk models for navier-stokes equation. **Europhysics Letters**, v. 17, n. 6, p. 479, feb 1992. Disponível em: https://doi.org/10.1209/0295-5075/17/6/001.

REYES, M. *et al*. Experimental study on the confined 3D laminar flow past a square prism with a high blockage ratio. **International Journal of Heat and Fluid Flow**, Elsevier Inc., v. 44, p. 444–457, 2013. ISSN 0142727X. Disponível em: http://dx.doi.org/10.1016/j.ijheatfluidflow.2013.08.001.

ROACHE, P. J. **Fundamentals of verification and validation**. [S.l.: s.n.], 2009. 476 p. ISBN 9780913478127.

ROHDE, M.; KANDHAI, D.; DERKSEN, J. J.; AKKER, H. E. Van den. A generic, mass conservative local grid refinement technique for lattice-boltzmann schemes. **International journal for numerical methods in fluids**, Wiley Online Library, v. 51, n. 4, p. 439–468, 2006.

ROMANI, G.; CASALINO, D. Application of lattice-boltzmann method to rotorcraft aerodynamics and aeroacoustics. *In*: **43rd European Rotorcraft Forum, ERF 2017**. [S.l.]: Associazione Italiana di Aeronautica e Astronautica (AIDAA), 2017. v. 2, p. 816–828. ISBN 9781510865389. 43rd European Rotorcraft Forum, ERF 2017 ; Conference date: 12-09-2017 Through 15-09-2017.

SCHULZ, M.; TÖLKE, J.; KRAFCZYK, M.; RANK, E. Parallel Single- and Multiphase CFD-Applications Using Lattice Boltzmann Methods. *In*: WAGNER, S.; BODE, A.; HANKE, W.; DURST, F. (Ed.). **High Performance Computing in Science and Engineering, Munich 2002**. Berlin, Heidelberg: Springer Berlin Heidelberg, 2003. p. 91–103. ISBN 978-3-642-55526-8.

SHAIR, F. *et al*. The effect of confining walls on the stability of the steady wake behind a circular cylinder. **Journal of Fluid Mechanics**, 1963.

SOHANKAR, A.; NORBERG, C.; DAVIDSON, L. Low-reynolds-number flow around a square cylinder at incidence: study of blockage, onset of vortex shedding and three-dimensional effects. **Journal of Wind Engineering and Industrial Aerodynamics**, v. 69–71, p. 189–201, 1998.

SUCCI, S. **The lattice Boltzmann equation: For fluid dynamics and beyond**. [S.l.]: Oxford University Press, 2013.

SUZUKI, H. *et al*. Unsteady flow in a channel obstructed by a square rod (crisscross motion of vortex). **International Journal of Heat Fluid Flow**, v. 14, n. 1, p. 2–9, 1993.

TEIXEIRA, C. M. Incorporating Turbulence Models into the Lattice-Boltzmann Method. **International Journal of Modern Physics C**, v. 09, n. 08, p. 1159–1175, 1998. Disponível em: https://doi.org/10.1142/S0129183198001060.

THOMPSON, P. A. **Compressible-Fluid Dynamics**. New York: McGraw-Hill, 1972.

TRAN, S. B. Q.; LEONG, F. Y.; LE, Q. T.; LE, D. V. Lattice Boltzmann Method for high Reynolds number compressible flow. **Computers Fluids**, v. 249, p. 105701, 2022. ISSN 0045-7930. Disponível em: https://www.sciencedirect.com/science/article/pii/S0045793022002948.

TURKI, S.; ABBASSI, H.; NASRALLAH, S. B. Effect of the blockage ratio on the flow in a channel with a built-in square cylinder. **Computational Mechanics**, v. 33, p. 22–29, 2003.

VICKERY, B. J. Fluctuating lift and drag on a long cylinder of square cross-section in a smooth and in a turbulent stream. **Journal of Fluid Mechanics**, 1966.

WANG, P. *et al*. A comparative study of lbe and dugks methods for nearly incompressible flows. **Communications in Computational Physics**, v. 17, n. 3, p. 657–681, mar. 2015.

WHITE, F. M. **Mecânica dos fluidos**. 8. ed. Porto Alegre: AMGH, 2016.

ZHAO-LI, G.; CHU-GUANG, Z.; BAO-CHANG, S. Non-equilibrium extrapolation method for velocity and pressure boundary conditions in the lattice boltzmann method. **Chinese physics**, IOP Publishing, v. 11, n. 4, p. 366, 2002.

ZHAO, T.; JI, Y. Gas Diffusion and Flow in Shale Nanopores with Bound Water Films. **Atmosphere**, v. 13, n. 6, 2022. ISSN 2073-4433. Disponível em: https://www.mdpi.com/2073-4433/13/6/940.

ZOU, Q.; HE, X. On pressure and velocity boundary conditions for the lattice Boltzmann BGK model. **Physics of Fluids**, v. 9, n. 6, p. 1591–1598, jun 1997. ISSN 1070-6631. Disponível em: http://arxiv.org/abs/comp-gas/9611001%0Ahttp://dx.doi.org/10.1063/1.869307http://aip.scitation.org/doi/10.1063/1.869307.

APPENDIX A – REPOSITORIES OF THE CODES USED

The codes uses in this work can be found in the GitHub Repository:

- https://github.com/poro-labcc/LBM-Thomas